The Astrophysical Journal Supplement Series, 245:24 (29pp), 2019 December https://doi.org/10.3847/1538-4365/ab5445

Electron Energy Partition across Interplanetary Shocks. II. Statistics

Lynn B. Wilson, III[1], Li-Jen Chen[1], Shan Wang[1,2], Steven J. Schwartz[3], Drew L. Turner[4], Michael L. Stevens[5], Justin C. Kasper[6], Adnane Osmane[7], Damiano Caprioli[8], Stuart D. Bale[9,10,11,12], Marc P. Pulupa[13], Chadi S. Salem[13], and Katherine A. Goodrich[13]

[1] NASA Goddard Space Flight Center, Heliophysics Science Division, Greenbelt, MD 20771, USA; lynn.b.wilsoniii@gmail.com
[2] Astronomy Department, University of Maryland, College Park, MD 20742, USA
[3] Laboratory for Atmospheric and Space Physics, University of Colorado, Boulder, Boulder, CO 80303, USA
[4] Space Sciences Department, The Aerospace Corporation, El Segundo, CA 90245, USA
[5] Harvard-Smithsonian Center for Astrophysics, Harvard University, Cambridge, MA 02138, USA
[6] University of Michigan, Ann Arbor, School of Climate and Space Sciences and Engineering, Ann Arbor, MI 48109, USA
[7] Department of Physics, University of Helsinki, Helsinki FI-00014, Finland
[8] Department of Astronomy and Astrophysics, University of Chicago, Chicago, IL 60637, USA
[9] Physics Department, University of California, Berkeley, CA 94720-7300, USA
[10] Space Sciences Laboratory, University of California, Berkeley, CA 94720-7450, USA
[11] The Blackett Laboratory, Imperial College London, London, SW7 2AZ, UK
[12] School of Physics and Astronomy, Queen Mary University of London, London E1 4NS, UK
[13] University of California Berkeley, Space Sciences Laboratory, Berkeley, CA 94720-7450, USA

Received 2019 September 20; revised 2019 October 29; accepted 2019 November 3; published 2019 December 6

Abstract

A statistical analysis of 15,210 electron velocity distribution function (VDF) fits, observed within ±2 hr of 52 interplanetary (IP) shocks by the *Wind* spacecraft near 1 au, is presented. This is the second in a three-part series on electron VDFs near IP shocks. The electron velocity moment statistics for the dense, low-energy core, tenuous, hot halo, and field-aligned beam/strahl are a statistically significant list of values illustrated with both histograms and tabular lists for reference and baselines in future work. Given the large statistics in this investigation, the beam/strahl fit results in the upstream are now the most comprehensive attempt to parameterize the beam/strahl electron velocity moments in the ambient solar wind. The median density, temperature, beta, and temperature anisotropy values for the core(halo)[beam/strahl] components, with subscripts ec(eh)[eb], of all fit results, respectively, are $n_{ec(h)[b]} \sim 11.3(0.36)[0.17]$ cm^{-3}, $T_{ec(h)[b],tot} \sim 14.6(48.4)[40.2]$ eV, $\beta_{ec(h)[b],tot} \sim 0.93(0.11)[0.05]$, and $\mathcal{A}_{ec(h)[b]} \sim 0.98(1.03)[0.93]$. This work will also serve as a 1 au baseline and reference for missions like *Parker Solar Probe* and *Solar Orbiter*.

Unified Astronomy Thesaurus concepts: Solar wind (1534); Interplanetary shocks (829); Solar coronal mass ejections (310); Solar coronal mass ejection shocks (1997); Space plasmas (1544); Plasma astrophysics (1261); Plasma physics (2089); Interplanetary particle acceleration (826)

1. Background and Motivation

The solar wind is a nonequilibrium, collisionless (or weakly collisional), ionized, kinetic gas that propagates away from the Sun at supersonic speeds (e.g., Kasper et al. 2006; Wilson et al. 2018, and references therein). The collisionless nature of the solar wind allows for anisotropic, non-Maxwellian, multicomponent velocity distribution functions (VDFs) to exist for periods long enough to be observed by in situ spacecraft (e.g., Feldman et al. 1975, 1978, 1979; Phillips et al. 1989a, 1989b; Lin 1998; Štverák et al. 2008, 2009; Wang et al. 2012; Scudder & Karimabadi 2013; Wicks et al. 2016; Horaites et al. 2018). The consistent, though not ubiquitous, electron heat flux is evidence that the solar wind is not in thermodynamic equilibrium and the temperatures of species s' and s are not equal, i.e., $(T_{s'}/T_s)_{tot} \neq 1$, for $s' \neq s$ (see Appendix A for parameter definitions). The temperature difference among particle species is consistently satisfied, which shows that the solar wind is rarely in thermal equilibrium as well (e.g., Feldman et al. 1973, 1975, 1978, 1979; Bame et al. 1979; Pilipp et al. 1990; Skoug et al. 2000; Maruca et al. 2011; Kasper et al. 2012, 2013; Maruca & Kasper 2013; Wilson et al. 2018, and references therein). Further, the recent observations of inelastic collisions (Wilson et al. 2019a), which had been tangentially discussed under different circumstances in previous theoretical work (e.g., Scudder & Olbert 1979), adds further evidence that the solar wind plasma is not in equilibrium.

The weakly collisional nature of the solar wind originally posed an issue as to whether shock waves could exist in such a medium (e.g., Petschek 1958; Kellogg 1962; Sagdeev 1966; Coroniti 1970). The subsequent observations of a shock-like boundary upstream of the Earth's magnetosphere showed that the ramp thickness—the spatial gradient scale length of the magnetic transition region—is often a few λ_e up to λ_p (e.g., Hobara et al. 2010; Mazelle et al. 2010, and references therein). The collisional mean free path of a typical proton near Earth is roughly 1 astronomical unit (au), whereas the typical corresponding thermal gyroradii (ρ_{cp}) and/or inertial length (λ_p) tend to satisfy ~50–150 km (e.g., Wilson et al. 2018, and references therein). Thus, the shock ramp thickness is orders of magnitude smaller than the collisional mean free path, which is why most astrophysical shocks are called collisionless.

The total distribution response—characterized by velocity moments—to a collisionless shock is often misleading (e.g., Wilson et al. 2013b) and not well correlated with any of the

observable macroscopic shock parameters (e.g., Wilson et al. 2007) except the change in bulk flow kinetic energy and some Mach number dependence (e.g., Wilson et al. 2009, 2010; Masters et al. 2011). This is largely the result of the energy-dependent processes responsible for converting the incident bulk flow into other forms like heat (see, e.g., Sagdeev 1966; Coroniti 1970; Tidman & Krall 1971; Kennel et al. 1985; Treumann 2009, and references therein), which can produce features like beams that are mischaracterized by velocity moments like the temperature. Further, recent high-resolution observations show that the evolution of the electron VDF through a collisionless shock is not a trivial, uniform inflation of the distribution, but a multistep process that deforms and redistributes/exchanges energy between the different electron components (e.g., Chen et al. 2018; Goodrich et al. 2018, 2019). However, there is no known way to quantify or parameterize these nuanced changes in a systematic way to examine a statistically significant set of shock crossings. Further, although the details of the electron VDF evolution are not entirely captured by the velocity moments of the electron components, nearly all theories describing the evolution of electron VDFs rely on either the velocity moments or a model VDF (e.g., Schunk 1975, 1977; Schwartz & Marsch 1983; Schwartz et al. 1988; Livadiotis 2015, 2017; Nicolaou et al. 2018; Shizgal 2018).

Finally, there is a dearth of statistical results for suprathermal electron velocity moments in the solar wind (for comparison to previous work and this work, see Appendix D for lists of electron parameters in tabular form), especially studies that separate the electron distribution into at least the three dominant components (e.g., Štverák et al. 2009): the cold, dense core with energies $E_{ec} \lesssim 15$ eV; the hot, tenuous halo with $E_{eh} \gtrsim 20$ eV; and the antisunward, field-aligned beam called the strahl with $E_{eb} \sim$ few $\times$ 10 eV. In the presence of strong collisionless shock waves, the strahl component can be contaminated with shock-reflected electrons. Thus, this component will be referred to as the beam/strahl component because the shock-reflected and ambient strahl electrons cannot be separated.

In this second part (Paper II) of this three-part study, the statistical analysis of the fit results to the multicomponent electron VDF analysis will be discussed. The results are summarized for the 52 IP shocks observed by the *Wind* spacecraft. The notation, symbols, and data sets used herein are the same as those in Wilson et al. (2019a, hereafter Paper I) and L. B. Wilson et al. (2019, in preparation, hereafter Paper III). The nuanced details of the fitting method and data product description were published in Paper I, and the detailed analysis of the results will be shown in Paper III. One of the primary purposes of this paper is to provide statistical references for the three primary electron component velocity moments. This is especially important for the beam/strahl component, as there have been very few studies providing details about the velocity moments near 1 au. This work will also serve as a 1 au baseline and reference for missions like *Parker Solar Probe* and *Solar Orbiter*.

This paper is outlined as follows: Section 2 introduces the data sets, statistical analysis techniques and procedures, selection criteria, and velocity moment numerical integration; Section 3 describes the statistical results through tables and histograms of the primary velocity moments examined herein; Section 4 introduces and discusses Coulomb collision estimates; Section 5 introduces and discusses the electron heat flux estimates; Section 6 summarizes the upstream only velocity moment statistics; and Section 7 presents the discussion and conclusions. We also include appendices that provide additional details for the reader on the parameter definitions (Appendix A), numerical velocity moment integration methodology (Appendix B), extra statistical tables and histograms (Appendix C) that show one-variable statistics separated by different selection criteria defined in Section 2, and a literature review of previous electron VDF studies in the near-Earth solar wind (Appendix D) for reference and direct comparison with the results presented herein.

2. Data Sets and Methodology

As in Paper I, all data are observed by instruments on the *Wind* spacecraft (Harten & Clark 1995) near 1 au. The data utilized include quasi-static magnetic field vectors ($\boldsymbol{B}_o$) from *Wind*/MFI (Lepping et al. 1995), electron and ion VDFs from *Wind*/3DP (Lin et al. 1995), and proton and alpha-particle velocity moments from the *Wind*/SWE Faraday Cups (Ogilvie et al. 1995; Kasper et al. 2006). The instrument details are described in Paper I. Parameters described with respect to $\boldsymbol{B}_o$ are in a field-aligned coordinate basis using a subscript j to denote the parallel ($j = \|$), the perpendicular ($j = \perp$), and total ($j =$ tot) directions. All electron parameters are shown with a subscript s denoting the component (or subpopulation) of the entire distribution, where $s =$ ec for the core, $s =$ eh for the halo, $s =$ eb for the beam/strahl, and $s = e$ for the entire distribution. The combined or mixed parameters (e.g., $\beta_{\mathrm{eff},j}$) use the subscripts $s =$ eff for *effective* and $s =$ int for *integrated* parameters (see Appendix A for definitions).

The VDF fit results are taken from additional supplemental material in the form of two ASCII files[14] found in Wilson et al. (2019b). In the following, data from tables show one-variable statistics of parameters from the electron VDF fit results, found within $\pm$2 hr of 52 IP shocks found in the *Wind* shock database from the Harvard Smithsonian Center for Astrophysics[15] between 1995 February 26 and 2000 February 20 (for a full list of event dates and times, see the PDF file included with additional supplemental material in Wilson et al. 2019b). The IP shocks examined were limited to fast-forward shocks[16] that had burst mode electron VDFs within the chosen time range about each shock.

The statistics shown in the tables are relative to the 15,210 VDFs examined herein, of which 14,418 had stable model fits ($f^{(\mathrm{core})}$) for the core, 13,660 had stable model fits ($f^{(\mathrm{halo})}$) for the halo, and 11,578 had stable model fits ($f^{(\mathrm{beam})}$) for the beam/strahl. Note that all statistics presented herein are for stable fits with a fit flag for the respective component of two or higher. The fit flags are defined in the appendices of Paper I and are provided in *File 1* of the additional supplemental material (Wilson et al. 2019b). Note that the software allows for solutions to be found for core only, the core and halo only, or the core and beam/strahl only. However, there are post-fit constraints and post-fit checks (e.g., examine ratio of model to data for "spiky" fits that are unphysical) imposed on the results that can eliminate a fit component while leaving the

[14] *File 1*: a fit results file containing all results used in Paper I with post-fit constraint failures set to fill values; *File 2*: a fit constraint file containing all results regardless of post-fit constraints or other disqualifying criteria.

[15] https://www.cfa.harvard.edu/shocks/wi_data/

[16] We do not discuss fast-reverse or any type of slow-mode shocks herein, which is beyond the scope of this work. Further, there are significantly more fast-forward shocks in the *Wind* shock database, allowing for a larger range of macroscopic shock parameters to sample.

other two alone; thus, some VDFs in *File 1* can have solutions to the core and beam/strahl or halo and beam/strahl. The post-fit constraints are $1.5 < \kappa_{eh} \leqslant 20$, $1.5 < \kappa_{eb} \leqslant 20$, $0 \leqslant n_{eh}/n_{ec} \leqslant 0.75$, $0 \leqslant n_{eb}/n_{ec} \leqslant 0.50$, $0.0 \leqslant n_{eb}/n_{eh} \leqslant 3.0$, $11.4\ \text{eV} \leqslant T_{eh,j} \leqslant 285\ \text{eV}$, and $11.4\ \text{eV} \leqslant T_{eb,j} \leqslant 285\ \text{eV}$. The justification and physical reasoning behind these constraints are discussed in detail in Paper I.

During the course of analysis, it was found that some of the post-fit constraints were eliminating otherwise valid fit beam/strahl results. Therefore, the combination of *File 1* and *File 2* from the supplemental material (Wilson et al. 2019b) was used to reintroduce valid fit component results. An example can be seen in Figure 6 of Paper I, where the fit results failed the post-fit criteria of $n_{eb}/n_{eh} \leqslant 3.0$ despite the beam/strahl fit being a perfectly valid numerical solution. Fit results like that shown in Figure 6 of Paper I are now included in the following discussion. These inappropriately removed fit results were found by searching for the following:

1. Fit Flag $\leqslant 0$; AND
2. Fit Status $\leqslant 0$ in *File 1* AND Fit Status > 0 in *File 2*; AND
3. ${\tilde{\chi}_{eb}}^2 \leqslant 10$ [from *File 2*]; AND
4. $(2 < \kappa_{eb} < 20)$ AND $(18\ \text{eV} < T_{eb,j} < 300\ \text{eV})$ [from *File 2*]; AND
5. $0.1\% \leqslant \delta\mathcal{R} < 80\%$; AND
6. $0 < {\tilde{\chi}_{tot}}^2 < 100$.

This resulted in an additional 2145 beam/strahl fits. There were an additional 46 core fits that had fill values for n_{ec} in *File 1* despite having otherwise valid fit parameters. Thus, the totals will differ slightly from those reported in Paper I.

The following selection criteria were also defined, while still requiring the fit flag lower bound of two, to further differentiate the fit results:

Criteria AT: All VDFs satisfying: Fit Flag $\{c, h, b\} \geqslant 2$ and no violation of post-fit constraints (AT is an abbreviation for All Times);
Criteria UP: All VDFs satisfying *Criteria AT* that were observed upstream of the IP shock ramp (UP is an abbreviation for Upstream Only Times);
Criteria DN: All VDFs satisfying *Criteria AT* that were observed downstream of the IP shock ramp (DN is an abbreviation for Downstream Only Times);
Criteria LM: All VDFs satisfying *Criteria AT* that were observed within ± 2 hr time window of shock ramp centers satisfying $\langle M_f \rangle_{up} < 3$ (LM is an abbreviation for Low Mach Number Shocks);
Criteria HM: All VDFs satisfying *Criteria AT* that were observed within ± 2 hr time window of shock ramp centers satisfying $\langle M_f \rangle_{up} \geqslant 3$ (HM is an abbreviation for High Mach Number Shocks);
Criteria PE: All VDFs satisfying *Criteria AT* that were observed within ± 2 hr time window of shock ramp centers satisfying $\theta_{Bn} > 45°$ (PE is an abbreviation for Quasi-perpendicular Shocks); and
Criteria PA: All VDFs satisfying *Criteria AT* that were observed within ± 2 hr time window of shock ramp centers satisfying $\theta_{Bn} \leqslant 45°$ (PA is an abbreviation for Quasi-parallel Shocks).

The total numbers of VDFs for each criterion for each component type (e.g., core) are shown in Table 1 for reference.

Table 1
Statistic of Stable Fits by Criteria

Type	AT	UP	DN	LM	HM	PE	PA
All	15,210	6546	8664	12,988	2222	10,940	4270
Core	14,418	6112	8306	12,405	2013	10,387	4031
Halo	13,660	5734	7926	11,738	1922	9888	3772
Beam	11,578	4977	6601	10,006	1572	8353	3225

Note. For symbol definitions, see Appendix A.

Note that unlike the Earth's bow shock, most quasi-parallel IP shocks exhibit a much more well-defined separation between upstream and downstream. Thus, *Criteria UP* and *Criteria DN* are still distinguishable and valid for the IP shocks examined herein. Despite the shock-parameter-dependent selection criteria, the purpose of this work is not to analyze the effects of the shocks on the components. However, one-variable statistics of the relevant electron fit parameters are presented in selection-criteria-separated tables in Appendix C. These values provide a 1 au reference/baseline for future work (for comparison to previous work, see tables in Appendix D). The tabular values presented in the main body of the paper are only for selection criteria *Criteria AT*. The analysis of the changes and dependencies of the electron fit parameters on the shock-parameter-dependent selection criteria will be presented in Paper III and is beyond the scope of this work.

The total/entire electron model VDF, $f_s^{(\text{mod})} = f^{(\text{core})} + f^{(\text{halo})} + f^{(\text{beam})}$, is used to define integrated velocity moments such as the parallel electron heat flux, $q_{e,\parallel}$, where the integration is performed using the Simpson's $\frac{1}{3}$ Rule algorithm. These integrations are only performed on VDFs where a stable solution for all three components was found and satisfying selection criteria *Criteria AT*. There are 10,983 VDFs that satisfy these criteria (see Appendix B for more details).

In the following one-variable statistics and histogram distributions of $T_{s,j}$, n_{es}, $n_{es}/n_{es'}$, $\beta_{s,j}$, $(T_{s'}/T_s)_j$, and $(T_\perp/T_\parallel)_{es}$ are presented (see Appendix A for parameter symbol definitions). The minimum (X_{min}), maximum (X_{max}), mean ($\bar{X}$), median ($\tilde{X}$), lower quartile ($X_{25\%}$), and upper quartile ($X_{75\%}$) are presented in Tables 2–6.

The histograms shown in Figures 1–5 present the number of events normalized to the number of finite values for that parameter for the specified selection criteria (e.g., *Criteria AT*). In some histograms, one or more of the parameters are shown with multiplicative offsets to reduce the range of the horizontal axis. All histograms were computed in linear space with uniform bin sizes for each parameter within any given panel. In some of the histograms, isolated peaks appear that should be regarded with caution rather than as having a physically significant interpretation. Some of these peaks arise because fit solutions contain results that lie on the boundary of an imposed constraint. For a full list of limits and constraints, see ASCII files provided in the additional supplemental material (Wilson et al. 2019b). Again, the justification and physical reasoning for imposing such constraints are explained in detail in Paper I.

3. Statistics of Electron Moments

In this section, the statistics of the electron velocity moments are presented both in tables of one-variable statistics and as histogram distributions.

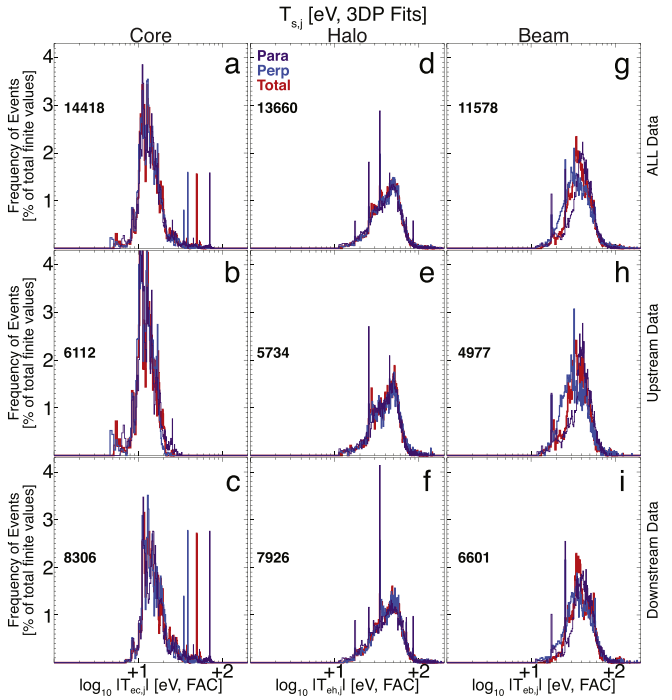

Figure 1. Temperatures (eV) for different electron components in each column and for the different regions (i.e., rows) listed in Table 2. In each panel, there are three color-coded histograms for the different field-aligned components defined as follows: total (red), parallel (violet), and perpendicular (blue). All histograms are normalized to the total number of finite points (i.e., black number in each panel) per parameter per component shown as a percentage.

Table 2
Temperature Parameters

Temp. (eV)	X_{min} [a]	X_{max} [b]	$\bar{X}$ [c]	$\tilde{X}$ [d]	$X_{25\%}$ [e]	$X_{75\%}$ [f]
Criteria AT: 15,210 VDFs						
$T_{ec,\parallel}$	5.67	89.1	19.1	15.0	12.1	19.1
$T_{ec,\perp}$	4.75	62.8	16.4	14.5	12.0	17.9
$T_{ec,tot}$	5.06	67.2	17.3	14.6	12.0	18.6
$T_{eh,\parallel}$	11.6	249	49.0	47.3	35.7	57.7
$T_{eh,\perp}$	11.4	255	50.7	48.7	37.2	58.6
$T_{eh,tot}$	11.6	222	50.2	48.4	37.4	58.1
$T_{eb,\parallel}$	11.5	280	44.2	42.8	36.2	51.4
$T_{eb,\perp}$	11.7	277	42.6	39.2	30.6	50.0
$T_{eb,tot}$	12.3	269	43.1	40.2	33.7	50.0
$T_{eff,\parallel}$	6.97	167	20.6	16.5	13.6	21.1
$T_{eff,\perp}$	4.93	170	18.1	15.8	13.4	19.8
$T_{eff,tot}$	5.61	169	18.9	16.0	13.6	20.5
$T_{int,\parallel}$	8.78	79.9	20.6	17.2	14.0	22.0
$T_{int,\perp}$	8.09	69.6	17.2	15.6	13.4	19.6
$T_{int,tot}$	8.41	69.1	18.3	16.1	13.7	20.4

Notes. For symbol definitions, see Appendix A.
[a] Minimum.
[b] Maximum.
[c] Mean.
[d] Median.
[e] Lower quartile.
[f] Upper quartile.

3.1. Electron Temperatures

In this section one-variable statistics and distributions of $T_{s,j}$ are introduced and discussed, for the core (s = ec), halo (s = eh), beam/strahl (s = eb), entire effective (s = eff), and entire integrated (s = int) distributions. The solar wind is a nonequilibrium, weakly collisional, kinetic gas; thus, the average kinetic energy in the species bulk flow rest frame more accurately describes the species temperature than a thermodynamic variable. Therefore, the temperatures are shown in units of eV rather than kelvin.

Table 2 shows the one-variable statistics for $T_{s,j}$ for *Criteria AT* only. Figure 1 shows the histograms of $T_{s,j}$ for all time periods, upstream only, and downstream only. For other selection criteria, Appendix C provides Table 8 and Figure 7.

First note that the $T_{eff,j}$ values in Tables 2 and 8 were computed using Equation 1(a) in Appendix A. The same one-variable statistics for the integrated electron temperatures (see Appendix B for details), $T_{int,j}$, are shown below $T_{eff,j}$ in Table 2. The integrated temperature one-variable statistics are all within a few percent of the effective values, except X_{min} and X_{max}, as further evidenced by the statistical differences illustrated in Appendix B. Thus, while the effective temperatures calculated from the fit results statistically represent the true temperature of the total VDF, the component values are of more interest as particle dynamics are intrinsically energy and pitch-angle dependent.

The $T_{ec,j}$ values change across the shock, which is expected since shocks heat and compress the media through which they propagate. The magnitude of the changes is most dramatic on the higher-temperature end of the histograms shown in Figures 1 and 7, which have significant high-end tails for every temperature component except for *Criteria UP*. In fact, the profile of the *Criteria UP* histogram in Figure 1 is similar to that of the total electron temperature in the solar wind reported in Wilson et al. (2018). Thus, the *Criteria UP* core parameters appear to be consistent with the ambient solar wind on a statistical basis.

The three large spikes in the $T_{ec,j}$ histograms in Figure 1(c) are entirely due to the following selection criteria: *Criteria DN*, *Criteria LM*, and *Criteria PE*. That is, they appear downstream of low Mach number, quasi-perpendicular shocks. However, the tail itself on top of which these spikes are superposed is present in the downstream of all shock types, but dominated by low and high Mach number, quasi-perpendicular shocks. That is, quasi-parallel shocks seem to be limited in generating large downstream core temperatures. The small peaks to the left of the main peak in Figure 1(a) are isolated to *Criteria UP*, *Criteria LM*, and *Criteria PE* shocks, as shown in Figures 1(b) and 7(b) and (d).

The $T_{eh,j}$ histograms are less symmetric and show a skewness toward lower values. The *Criteria UP* histograms show a bimodal distribution that is dominated by *Criteria LM* and *Criteria PE* shocks. The *Criteria HM* shocks show a different bimodal distribution, i.e., peaks at different values, and generally higher values of $T_{eh,j}$. Interestingly, the histograms for *Criteria UP* and *Criteria DN* share the same higher-temperature peak, but the latter lacks the lower-temperature peak. This leads to the one-variable statistics

values being slightly larger for *Criteria DN*, but only slightly. The biggest difference in one-variable statistics is shown in Table 8 between *Criteria LM* and *Criteria HM* shocks. This is somewhat expected, as stronger shocks are predicted to be more efficient particle accelerators and the efficiency increases with increasing particle energy (e.g., Caprioli & Spitkovsky 2014; Park et al. 2015). Otherwise, the halo temperature histograms and one-variable statistics are remarkably stable between the different selection criteria.

The $T_{\mathrm{eb},j}$ histograms are even stabler among the selection criteria in one-variable statistics, with the only clear differences occurring between *Criteria PA* and *Criteria PE* shocks, but it is a rather weak difference compared to other electron VDF parameters discussed in this work. This seems to contradict a clear difference in the $T_{\mathrm{eb},\perp}$ histogram profiles among the various selection criteria, which is clearly different in Figures 1(h) and (i) and 7(l)–(o). What is likely contributing to the lower $T_{\mathrm{eb},\perp}$ values in the *Criteria UP* histograms is shock-reflected electrons, which are more field aligned than the nominal solar wind strahl. This would skew the normal anisotropy in the beam component toward lower $T_{\mathrm{eb},\perp}$ and higher $T_{\mathrm{eb},\parallel}$ values. The most dramatic difference between $T_{\mathrm{eb},\perp}$ and $T_{\mathrm{eb},\parallel}$ histograms is for *Criteria PA* shocks seen in Figure 7(o). This is apparent in the one-variable statistics values in Table 8.

In summary, it is difficult to diagnose the source of the differences and similarities for each electron component temperature between opposing selection criteria because the populations can change components and sometimes overlap. For instance, upstream core electrons can become energized by a shock and enter what is modeled as the halo in the downstream. It is not possible to distinguish between the two or track particles, but it is possible to gain a statistical basis for the partition of random kinetic energy between the three electron components examined herein. In short, the core electrons receive the largest amount of energy across the IP shocks examined, the halo electrons respond well to high Mach number shocks, and the beam/strahl electrons only show clear differences between quasi-parallel and quasi-perpendicular in $T_{\mathrm{eb},\perp}$ and $T_{\mathrm{eb},\parallel}$. A detailed examination of the dependencies of $T_{s,j}$ on various macroscopic shock parameters will be presented in Paper III.

3.2. Number Densities

In this section one-variable statistics and distributions of n_s and $n_s/n_{s'}$ are introduced and discussed, where s = ec, eh, eb, eff, and int for the electrons and $s = p$ (protons), α (alpha-particles), and i (all ions) for the ions.

Table 3 shows the one-variable statistics for n_s and $n_s/n_{s'}$ (for electrons and ions) for all time periods only (see Table 9 and Figure 9 in Appendix C for other selection criteria). Figure 8 shows the histograms of n_s (ions and electrons) and $n_s/n_{s'}$ (electrons only).

Note that the n_{eff} values in Table 3 were computed by summing the fit results, i.e., $n_{\mathrm{eff}} = n_{\mathrm{ec}} + n_{\mathrm{eh}} + n_{\mathrm{eb}}$. The same one-variable statistics for the integrated electron densities (see Appendix B for details), $n_{e,\mathrm{int}}$, are shown just below n_{eff} in Table 3. As one can see, these results are consistent with the summed moment values shown in Table 3.

The ion densities in Figures 2 and 8 are included as a reference, though not the focus of this work. The histograms of n_p and n_i are both bimodal and peak at roughly the same values,

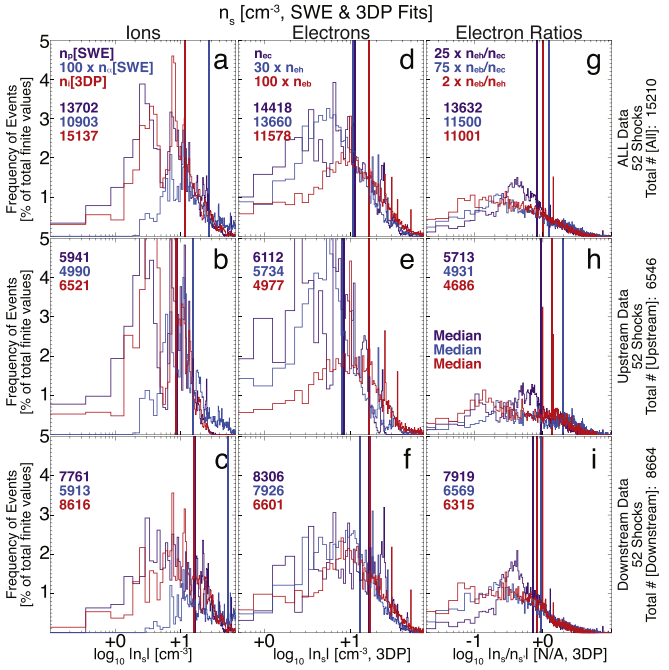

Figure 2. Densities (cm^{-3}) and density ratios for different ion and electron components as a percentage of the total number of finite points (i.e., color-coded numbers in each panel). The format is similar to Figure 1 with the row organization, but the columns differ. The first column here shows proton (violet) and alpha-particle (blue) density from *Wind*/SWE and total ion density from *Wind*/3DP (red). The second column shows n_{es} for the core (violet), halo (blue), and beam/strahl (red) components. The third column shows $n_s/n_{s'}$ for the halo-to-core (violet), beam-to-core (blue), and beam-to-halo (red) density ratios. The corresponding one-variable statistics for the electron parameters are shown in Table 3. Note that the n_α, n_{eh}, n_{eb}, and all three $n_s/n_{s'}$ values were offset by constant factors (shown in panels (a), (d), and (g)) to reduce the horizontal axis dynamic range.

Table 3
Density Parameters

n_s (cm^{-3})	X_{min}[a]	X_{max}	$\bar{X}$	$\tilde{X}$	$X_{25\%}$	$X_{75\%}$
Criteria AT: 15,210 VDFs						
n_p	0.10	76.2	14.8	11.7	6.43	21.5
n_α	0.02	4.75	0.45	0.28	0.13	0.66
n_i	0.18	98.8	15.5	11.5	7.19	19.9
n_{ec}	0.30	55.3	13.8	11.3	6.55	19.4
n_{eh}	0.002	6.87	0.51	0.36	0.20	0.63
n_{eb}	0.0009	3.50	0.24	0.17	0.10	0.29
n_{eff}	0.004	56.9	14.4	11.9	6.92	20.3
n_{int}	0.39	56.9	14.6	12.1	7.30	20.4
$n_{\mathrm{eh}}/n_{\mathrm{ec}}$	0.0002	0.30	0.05	0.03	0.02	0.06
$n_{\mathrm{eb}}/n_{\mathrm{ec}}$	0.00003	0.30	0.03	0.02	0.008	0.04
$n_{\mathrm{eb}}/n_{\mathrm{eh}}$	0.002	9.86	0.82	0.50	0.24	0.96

Notes. For symbol definitions, see Appendix A.
[a] Header symbols match those of Table 2.

showing consistency between the two independent measurements from *Wind* SWE and 3DP. The slight offset toward higher values for n_i results from it including the alpha-particle densities, i.e., it is the total ion number density. Note that the peaks of n_p and n_i are both near the same values as the bimodal peaks in n_{ec}, adding evidence to the accuracy of the fit results already presented in Paper I. The ion densities are not the focus, and further discussion is beyond the scope of this work.

The n_{ec} values change across the shock ramp, as expected since a shock compresses the fluid density and the core is representative of the bulk of the electron VDF. The magnitude of the change between *Criteria UP* and *Criteria DN* (Figures 2(e) and (f)) is consistent with those for n_p and n_i (Figures 2(b) and (c)) and those expected from the Rankine–Hugoniot conservation relations, within uncertainties, for each event (see supplemental PDF in Wilson et al. 2019b, for a list of compression ratios). The only selection criteria difference that may be somewhat surprising is that between *Criteria PE* and *Criteria PA* shocks. All one-variable statistic values of n_{ec}, except X_{min}, are larger for *Criteria PE* than *Criteria PA* shocks. This effect is clearly dominated by the *Criteria DN* values as evidenced by the similar profiles in Figures 2(e) and 8(j) and between Figures 2(f) and 8(i). Again, this is not tremendously surprising, as the density compression ratio for quasi-parallel shocks is lower than that for quasi-perpendicular ones. In summary, the core electron densities behave as one would expect across IP shocks.

The n_{eh} values also show compression across the shock, but to a lesser extent than n_{ec}. Although the one-variable statistics for n_{ec} did not show a tremendous difference between *Criteria LM* and *Criteria HM* shocks, n_{eh} is clearly higher for *Criteria HM* shocks. This may result from the higher temperatures observed at *Criteria HM* shocks, causing some core electrons to be included in the halo fits, or it may indicate that the halo responds more to stronger shocks. The latter is likely, as stronger shocks are more efficient at accelerating particles and the efficiency increases with increasing particle energy (e.g., Caprioli & Spitkovsky 2014; Park et al. 2015). That is, stronger shocks produce more suprathermal electrons, which result in larger n_{eh} fit values.

The n_{eb} values are effectively the same between *Criteria UP* and *Criteria DN* shocks and only slightly different between *Criteria PE* and *Criteria PA* shocks. The n_{eb} values do show larger values at *Criteria HM* than *Criteria LM* shocks, but again the differences are small compared to those for n_{ec} and n_{eh}. Thus, the beam/strahl electron densities do not seem to be strongly dependent on any macroscopic shock parameter or on the shock region. This might result from their nearly field-aligned pitch-angle distribution, which reduces the effects of magnetic field gradients on their dynamics.

In summary, similar to the $T_{s,j}$, the core shows the strongest dependence on *Criteria UP* versus *Criteria DN* and all other selection criteria. The beam/strahl densities are also somewhat indifferent to the selection criteria, much like the associated temperatures with the halo showing mostly weak dependencies.

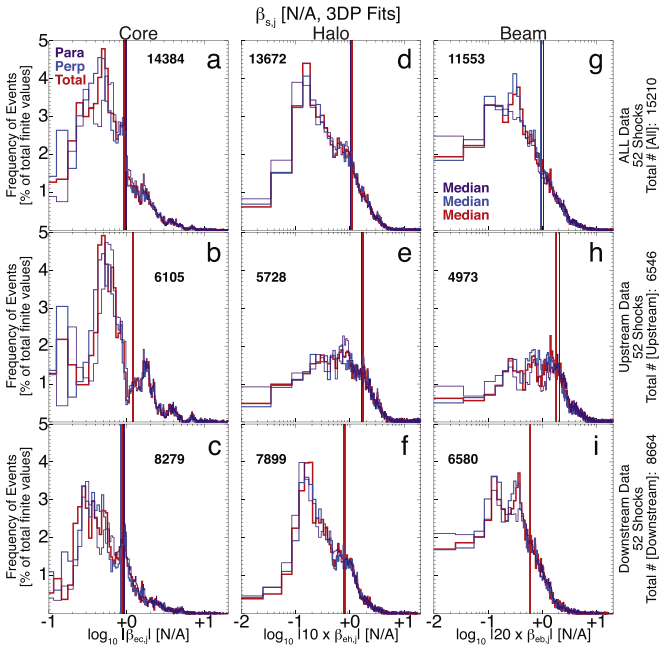

Figure 3. Same format as Figures 1 and 2, except for electron betas (N/A). Note that all $\beta_{eh,j}$ and $\beta_{eb,j}$ values were offset by constant factors of 10 and 20, respectively, to reduce the horizontal axis dynamic range.

Table 4
Electron Beta Parameters

$\beta_{s,j}$ (N/A)	X_{min}[a]	X_{max}	$\bar{X}$	$\tilde{X}$	$X_{25\%}$	$X_{75\%}$
Criteria AT: 15,210 VDFs						
$\beta_{ec,\parallel}$	0.05	3313	3.62	0.97	0.58	2.03
$\beta_{ec,\perp}$	0.04	3268	3.51	0.91	0.49	2.01
$\beta_{ec,tot}$	0.05	3283	3.54	0.93	0.52	2.01
$\beta_{eh,\parallel}$	0.0001	375	0.48	0.10	0.05	0.22
$\beta_{eh,\perp}$	0.0008	378	0.49	0.11	0.05	0.22
$\beta_{eh,tot}$	0.0009	377	0.49	0.11	0.05	0.22
$\beta_{eb,\parallel}$	0.00002	33.7	0.13	0.05	0.02	0.11
$\beta_{eb,\perp}$	0.00003	46.4	0.12	0.05	0.02	0.10
$\beta_{eb,tot}$	0.00003	42.0	0.12	0.05	0.02	0.10
$\beta_{eff,\parallel}$	0.0009	3721	4.15	1.12	0.69	2.28
$\beta_{eff,\perp}$	0.0010	3693	4.04	1.04	0.60	2.25
$\beta_{eff,tot}$	0.0009	3702	4.08	1.06	0.63	2.26

Notes. For symbol definitions, see Appendix A.
[a] Header symbols match those of Table 2.

3.3. Electron Betas

In this section one-variable statistics and distributions of plasma betas, $\beta_{s,j}$, are introduced and discussed, where s = ec, eh, eb, and eff and $j = \parallel$ (parallel), $\perp$ (perpendicular), and tot (total).

Table 4 shows the one-variable statistics for $\beta_{s,j}$ for all time periods only. Figure 3 shows the histograms of $\beta_{s,j}$ (see Table 10 and Figure 9 in Appendix C for other selection criteria).

The $\beta_{ec,j}$ values are much stabler than the $\beta_{eh,j}$ or $\beta_{eb,j}$ between the different selection criteria, but even so the one-variable statistic values can differ by over 100%. The $\beta_{ec,j}$ histograms in Figure 3 show a bimodal distribution for selection criteria *Criteria UP* and *Criteria DN*, but the peaks occur at lower values for *Criteria DN*. The bimodal profile of the $\beta_{ec,j}$ histograms for *Criteria UP* occurs upstream of low Mach number, quasi-parallel shocks, whereas the bimodal profile for *Criteria DN* occurs downstream of high Mach number, quasi-perpendicular shocks.

Unlike $\beta_{ec,j}$, the histograms for *Criteria UP* and *Criteria DN* are completely different in profile for both $\beta_{eh,j}$ and $\beta_{eb,j}$. That is, the *Criteria UP* histograms for both $\beta_{eh,j}$ and $\beta_{eb,j}$ are broad with weak peaks, while the *Criteria DN* histograms show similar profiles to those for selection criteria *Criteria AT*. For both suprathermal components, the *Criteria UP* histograms are

skewed toward higher values than the *Criteria DN* histograms. When looking at the other selection criteria histograms shown in Figure 9 (in Appendix C), the profiles of the *Criteria AT* $\beta_{s,j}$ histograms are clearly dominated by the low Mach number and quasi-perpendicular shock results, which is likely due to the significantly larger fraction of VDFs satisfying selection criteria *Criteria LM* and *Criteria PE*. However, there is no clear selection criteria differences in Figure 9 to explain the upstream/downstream histogram differences in Figure 3. Thus, the difference appears to solely rely on the region of observation near the shock, not the shock strength or geometry. Yet despite the apparent lack of dependence on the shock parameters, the one-variable statistic values can differ by over 300% between any two opposing selection criteria for both $\beta_{\mathrm{eh},j}$ and $\beta_{\mathrm{eb},j}$.

Therefore, the $\beta_{\mathrm{ec},j}$ values are stabler between any two opposing selection criteria than either $\beta_{\mathrm{eh},j}$ or $\beta_{\mathrm{eb},j}$, and both $\beta_{\mathrm{eh},j}$ and $\beta_{\mathrm{eb},j}$ depend on all selection criteria. That is, the histogram profiles and one-variable statistics can be wildly different between *Criteria UP* and *Criteria DN*, *Criteria LM* and *Criteria HM*, and *Criteria PE* and *Criteria PA*. A detailed examination of the changes and dependencies in $\beta_{s,j}$ will be explored in greater detail in Paper III and is beyond the scope of this work.

3.4. Electron Temperature Ratios

In this section one-variable statistics and distributions of the electron temperature ratios (see Appendix A for parameter definitions) for the core (s = ec), halo (s = eh), beam/strahl (s = eb), and entire effective (s = eff) distributions are presented.

Table 5 shows the one-variable statistics for $\mathcal{T}^{s'}_{s\,j} = (T_{s'}/T_s)_j$ for all time periods only. Figure 4 shows the histograms of $\mathcal{T}^{s'}_{s\,j}$ (see Table 11 and Figure 10 in Appendix C for other selection criteria).

In Figures 4 and 10 one can see that the temperature ratios dependent on the core (i.e., first two columns) show a tail toward lower values clearly occurring in the downstream (i.e., *Criteria DN*). This is largely because the halo and beam/strahl are less dependent on the region than the strength and geometry. The large tails appear to be predominantly at shocks satisfying *Criteria DN* and *Criteria PA* (i.e., $\theta_{\mathrm{Bn}} \leqslant 45°$ shocks) for $\mathcal{T}^{\mathrm{eh}}_{\mathrm{ec}\,j}$. There are tails for both *Criteria LM* and *Criteria HM* shocks, but they are more important in *Criteria HM* shocks. Notice that $\mathcal{T}^{\mathrm{eh}}_{\mathrm{ec}\perp}$ is bimodal but $\mathcal{T}^{\mathrm{eh}}_{\mathrm{ec}\parallel}$ is trimodal for *Criteria DN*. This two- versus three-peak histogram form appears as well for *Criteria PA*, suggesting that the profile results from quasi-parallel shocks and occurs in the downstream.

Interestingly, the tails at small values for $\mathcal{T}^{\mathrm{eb}}_{\mathrm{ec}\,j}$ are more nuanced. Again, they occur in the downstream but for both *Criteria LM* and *Criteria HM* in addition to both *Criteria PE* and *Criteria PA* shocks. The nuance is that there are clear peaks at low values for *Criteria HM* and *Criteria PA* shocks near ~0.4–0.5 and ~0.9–1.0, respectively. For reference, the dominant peaks of the histograms are up in the ~1.8–3.0 range for all selection criteria for $\mathcal{T}^{\mathrm{eb}}_{\mathrm{ec}\,j}$. The $\mathcal{T}^{\mathrm{eb}}_{\mathrm{ec}\parallel}$ histograms are bimodal for both *Criteria HM* and *Criteria PA* shocks. The $\mathcal{T}^{\mathrm{eb}}_{\mathrm{ec}\perp}$ histograms are bimodal for *Criteria PA* shocks but trimodal for *Criteria HM* shocks.

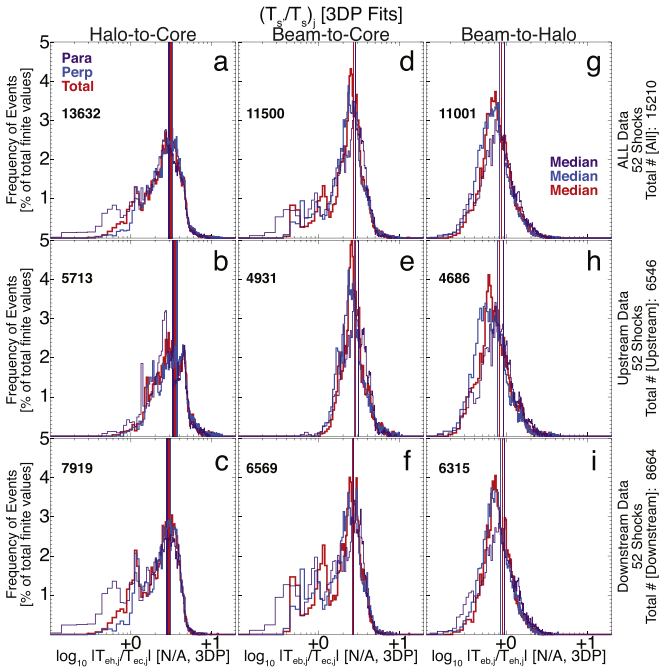

Figure 4. Same format as Figures 1 and 2, except for electron temperature ratios (N/A).

Table 5
Electron Temperature Ratio Parameters

Ratio	X_{min}[a]	X_{max}	$\bar{X}$	$\tilde{X}$	$X_{25\%}$	$X_{75\%}$
Criteria AT: 15,210 VDFs						
$\mathcal{T}^{\mathrm{eh}}_{\mathrm{ec}\parallel}$	0.17	17.9	3.11	3.02	2.21	3.97
$\mathcal{T}^{\mathrm{eh}}_{\mathrm{ec}\perp}$	0.41	17.9	3.40	3.27	2.45	4.10
$\mathcal{T}^{\mathrm{eh}}_{\mathrm{ec\,tot}}$	0.34	16.3	3.29	3.20	2.39	4.04
$\mathcal{T}^{\mathrm{eb}}_{\mathrm{ec}\parallel}$	0.23	25.7	2.86	2.85	2.09	3.54
$\mathcal{T}^{\mathrm{eb}}_{\mathrm{ec}\perp}$	0.46	24.6	2.88	2.69	2.12	3.38
$\mathcal{T}^{\mathrm{eb}}_{\mathrm{ec\,tot}}$	0.42	25.0	2.86	2.73	2.22	3.35
$\mathcal{T}^{\mathrm{eb}}_{\mathrm{eh}\parallel}$	0.15	6.12	1.06	0.93	0.69	1.30
$\mathcal{T}^{\mathrm{eb}}_{\mathrm{eh}\perp}$	0.13	7.11	0.95	0.81	0.61	1.11
$\mathcal{T}^{\mathrm{eb}}_{\mathrm{eh\,tot}}$	0.17	6.08	0.97	0.85	0.66	1.14
$\mathcal{T}^{\mathrm{eh}}_{\mathrm{eff}\parallel}$	0.17	17.4	2.80	2.73	2.03	3.57
$\mathcal{T}^{\mathrm{eh}}_{\mathrm{eff}\perp}$	0.43	16.8	3.03	2.95	2.24	3.69
$\mathcal{T}^{\mathrm{eh}}_{\mathrm{eff\,tot}}$	0.37	15.2	2.94	2.88	2.17	3.64
$\mathcal{T}^{\mathrm{eb}}_{\mathrm{eff}\parallel}$	0.24	19.6	2.56	2.57	1.89	3.17
$\mathcal{T}^{\mathrm{eb}}_{\mathrm{eff}\perp}$	0.46	18.7	2.57	2.37	1.91	3.02
$\mathcal{T}^{\mathrm{eb}}_{\mathrm{eff\,tot}}$	0.43	19.0	2.57	2.44	1.99	3.03

Notes. For symbol definitions, see Appendix A.
[a] Header symbols match those of Table 2.

The $\mathcal{T}^{\mathrm{eb}}_{\mathrm{eh}\,j}$ histograms are stabler between the various selection criteria. One can see that $\mathcal{T}^{\mathrm{eb}}_{\mathrm{eh}\perp}$ consistently has a peak at smaller values than $\mathcal{T}^{\mathrm{eb}}_{\mathrm{eh}\parallel}$ for all selection criteria except *Criteria HM*.

3.5. Electron Temperature Anisotropies

In this section one-variable statistics and distributions of the electron temperature anisotropy (see Appendix A for parameter definitions) for the core (s = ec), halo (s = eh), beam/strahl (s = eb), and entire effective (s = eff) distributions are presented.

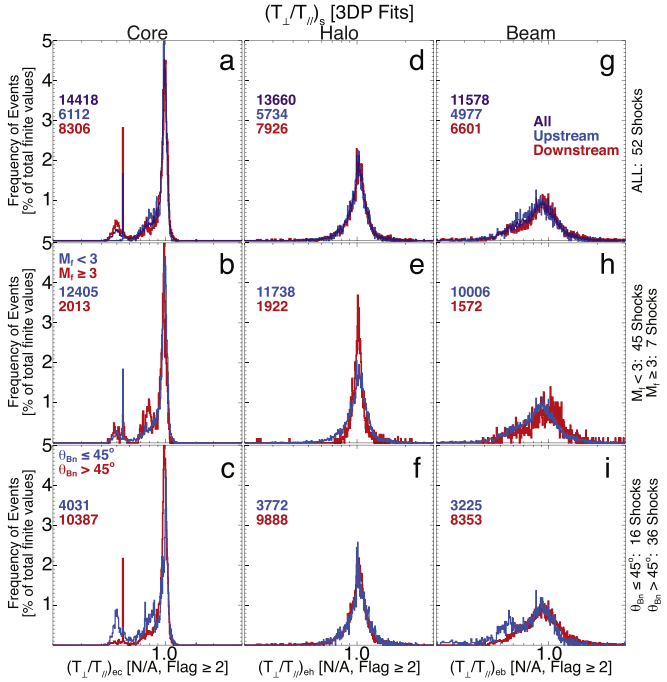

Figure 5. Temperature anisotropies (N/A) for different electron components in each column for different regions and shock parameters (i.e., color-coded labels by row). The top row shows all (violet), upstream (blue), and downstream (red) anisotropies. The middle row shows low Mach number (blue) and high Mach number (red) anisotropies. The bottom row shows quasi-parallel (blue) and quasi-perpendicular (red) anisotropies.

Table 6
Electron Temperature Anisotropy Parameters

Anisotropy	X_{min} [a]	X_{max}	$\tilde{X}$	$\tilde{X}$	$X_{25\%}$	$X_{75\%}$
Criteria AT: 15,210 VDFs						
$\mathcal{A}_{ec}$	0.38	1.56	0.93	0.98	0.90	1.01
$\mathcal{A}_{eh}$	0.24	15.0	1.06	1.03	0.95	1.12
$\mathcal{A}_{eb}$	0.13	15.2	1.00	0.93	0.78	1.11
$\mathcal{A}_{eff}$	0.35	2.80	0.93	0.98	0.91	1.01

Notes. For symbol definitions, see Appendix A.
[a] Header symbols match those of Table 2.

Table 6 shows the one-variable statistics for $\mathcal{A}_s = (T_\perp/T_\parallel)_s$ for all time periods only (see Table 12 in Appendix C for other selection criteria). Figure 5 shows the histograms of $\mathcal{A}_s$. Note that Figure 5 differs from previous histograms herein because the smaller number of parameters allows for the presentation of all selection criteria to be plotted simultaneously for all three electron components.

A quick examination of Figure 5 shows a bimodal distribution in $\mathcal{A}_{ec}$ for all selection criteria. The smaller $\mathcal{A}_{ec}$ peak corresponds to stronger parallel than perpendicular heating downstream of shocks (i.e., *Criteria DN*), as evidenced by the red line in Figure 5(a). The bimodal dependence appears to be more strongly dependent on θ_{Bn} than $\langle M_f \rangle_{up}$, where the peak near ~0.5 is clearly dominant for *Criteria PA* shocks in Figure 5(c). The $\langle M_f \rangle_{up}$ appears to be a little more complicated, as the distribution is trimodal in Figure 5(b) for *Criteria HM* shocks. The 5th and 95th percentile values for $\mathcal{A}_{ec}$ are ~0.42 and ~1.21, respectively. From the quartiles, one can see that only ~25% fell below ~0.85 or above ~0.99. Note that $\mathcal{A}_{eff}$ is dominated by the core and so has similar dependencies to that of $\mathcal{A}_{ec}$. In summary, the core electrons tend toward isotropy and only appear to strongly deviate from that downstream of high Mach number and/or quasi-parallel shocks.

The halo shows a larger total range of $\mathcal{A}_{eh}$ and more values satisfying $\mathcal{A}_{eh} > 1.0$, but the distributions are strongly peaked near unity as shown in Figures 5(d)–(f). The distributions show little or no dependence on θ_{Bn} in Figure 5(f) and Table 12, but there do appear to be stronger tails for *Criteria LM* shocks in Figure 5(e) and Table 12. That is, there is a statistically larger range of $\mathcal{A}_{eh}$ for low Mach number shocks. However, the general shapes of the histogram distributions in Figures 5(d)–(f) are the same for each selection criterion, suggesting that the shock itself has little to do with affecting or regulating the halo temperature anisotropy. This could imply that some other mechanism is responsible, as suggested in previous work, like whistler and/or firehose modes (Wilson et al. 2013b; Roberg-Clark et al. 2018; Tong et al. 2019b; Vasko et al. 2019). Thus, this may suggest that only instabilities and/or turbulence significantly affect the halo temperature anisotropy and electron heat flux in the solar wind, not the IP shocks.

Finally, the distributions of $\mathcal{A}_{eb}$ seem to show more variation and dependence on the macroscopic shock parameters. One can see that $\mathcal{A}_{eb}$ also exhibits a bimodal distribution for *Criteria PA* shocks in Figure 5(i), similar to $\mathcal{A}_{ec}$, though the peaks are at different locations. The distribution also appears to skew toward smaller $\mathcal{A}_{eb}$ for *Criteria LM* shocks than the converse in Figure 5(h). That is, higher Mach number shocks have statistically larger $\mathcal{A}_{eb}$ than the converse. The same is true for quasi-perpendicular shocks than the quasi-parallel shocks. That is, high Mach number, quasi-perpendicular shocks show larger $\mathcal{A}_{eb}$ than the converse, suggesting that perpendicular scattering is more efficient in these shocks for the beam/strahl component. It is not clear whether the shock is directly responsible for these differences or the responsible mechanism finds the environment surrounding these types of shocks more conducive for existence and/or affecting the beam/strahl electrons. A possible explanation for the larger anisotropy near high Mach number and/or quasi-perpendicular shocks is that the beam/strahl component is more likely contaminated with foreshock electrons, which would have larger pitch angles near the shock owing to processes like fast Fermi acceleration (e.g., Leroy & Mangeney 1984; Wu 1984; Krauss-Varban & Wu 1989) and/or shock drift acceleration (e.g., Ball & Melrose 2001; Lever et al. 2001; Vandas 2001). However, these same mechanisms could only generate field-aligned beams far upstream of the shock, along the quasi-static magnetic field similar to the terrestrial electron foreshock edge (e.g., Anderson et al. 1979; Anderson 1981).

A slightly different view of the temperature anisotropy statistics can be seen in Figure 11 in Appendix C. The anisotropies of each electron component are plotted versus the parallel electron beta of each electron component. Note that the results in the diagonal panels are consistent with previous observations (e.g., Štverák et al. 2008; Adrian et al. 2016). However, a detailed examination of the changes in $\mathcal{A}_s$ is beyond the scope of this work and will be examined in Paper III.

4. Coulomb Collision Rates

In this section one-variable statistics of the Coulomb collision rates (see Appendix A for parameter definitions) between the electron components—core (s = ec), halo (s = eh), beam/strahl (s = eb)—and protons ($s = p$) and alpha-particles ($s = \alpha$) are presented.

Calculating the Coulomb collision rates between different electron components and different species is important for verifying that indeed a variation or range of parameters is not

Table 7
Coulomb Collision Rates [# per Week]

$\nu_{ss'}$	$X_{\min}$ [a]	$X_{\max}$	$\bar{X}$	$\tilde{X}$	$X_{25\%}$	$X_{75\%}$
Criteria AT: 15,210 VDFs						
$\nu_{p\alpha}$	0.0003	0.52	0.02	0.01	0.008	0.02
ν_{ebb}	0.00007	1.42	0.03	0.02	0.008	0.03
ν_{ehh}	0.00006	3.14	0.05	0.03	0.01	0.06
ν_{ehb}	0.00008	8.76	0.07	0.03	0.02	0.07
$\nu_{eh\alpha}$	0.0008	1.53	0.08	0.04	0.02	0.10
$\nu_{eb\alpha}$	0.003	1.55	0.09	0.05	0.02	0.12
$\nu_{\alpha\alpha}$	0.002	1.60	0.12	0.06	0.02	0.14
$\nu_{ec\alpha}$	0.009	3.11	0.35	0.23	0.12	0.48
ν_{pp}	0.0001	3.97	0.53	0.30	0.10	0.74
ν_{ehp}	0.004	16.1	0.63	0.49	0.23	0.80
ν_{ebp}	0.004	8.78	0.70	0.52	0.29	0.90
ν_{ehc}	0.02	49.3	2.37	1.75	0.79	2.79
ν_{ebc}	0.02	57.8	4.68	2.18	1.08	3.90
ν_{ecp}	0.009	14.7	2.99	2.64	1.17	4.27
ν_{ecc}	0.05	22.3	5.45	4.80	2.23	7.81

Notes. For symbol definitions, see Appendix A.
[a] Header symbol definitions match those of Table 2.

solely due to differences in solar wind. Using Equations 2(a)—3(f), the collision rates, $\nu_{ss'}$, between species s and s' can be approximated for the different selection criteria discussed herein.

Table 7 shows the one-variable statistics for $\nu_{ss'}$ [# week^{-1}][17] for all time periods only sorted, from smallest to largest, by the $\tilde{X}$ values. The values for the other selection criteria can be found in Appendix C in Table 13. The median values all fall below 8×10^{-6} # s^{-1}, while the upper quartile values fall below 1×10^{-4} # s^{-1}, consistent with previous statistical work (e.g., Wilson et al. 2018).

The $\tilde{X}$ values for the rms mean free path (Equation (4)) range from ~0.57 au (astronomical unit) for $\lambda_{pp}{}^{mpf}$ to ~869 au for $\lambda_{ebb}{}^{mpf}$ (the smallest $\bar{X}$ for all rates is ~5 au). Note that proton–proton interactions are the only ones that have $\lambda_{ss'}{}^{mpf} < 1.0$ au. Further, the medians that satisfy $\leqslant$5.0 au are, from smallest to largest, $\lambda_{pp}{}^{mpf} \sim 0.57$ au, $\lambda_{\alpha\alpha}{}^{mpf} \sim 1.36$ au, $\lambda_{ecc}{}^{mpf} \sim 1.92$ au, and $\lambda_{ecp}{}^{mpf} \sim 2.23$ au.

Note that although the values of $\nu_{ss'}$ with either $s = c$ or $s' = c$ tend to be larger than the rates not involving the core electrons, they are still very slow. For instance, the largest $\nu_{ss'}$ value is between beam/strahl and core electrons at ~58/week, but that is still only $\sim 10^{-4}$ # s^{-1}, i.e., only ~8 collisions per day. Further, ~75% of all ν_{ebc} values are at or below ~0.56 # day^{-1}. If Coulomb collision rates between core electrons and any other species were higher, the core would relax to a bi-Maxwellian. However, it is interesting that ~80.5% satisfied $2.00 \leqslant s_{ec} \leqslant 2.05$ despite the low collision rates with core electrons. This may imply some remnant property of the solar atmosphere where collision rates are much higher or where preferential heating takes place (e.g., Marsch 2006; Kasper et al. 2017; Kasper & Klein 2019).

5. Electron Heat Flux

In this section one-variable statistics of the parallel electron heat flux, $q_{e,\parallel}$ (see Appendix A for parameter definitions), for the entire model electron VDF fits and the normalized heat flux, $q_{e,\parallel}/q_{eo}$, are presented. The integration performed to compute

[17] Divide by 604,800 to convert to # s^{-1}.

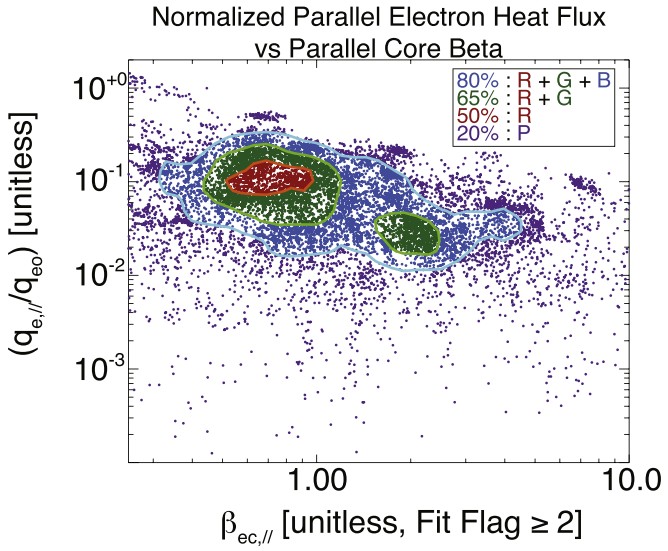

Figure 6. Normalized parallel electron heat flux, $q_{e,\parallel}/q_{eo}$ (N/A), vs. parallel core electron beta, $\beta_{ec,\parallel}$ (N/A). The color-coded contours (legend in upper right corner) are generated from a two-dimensional histogram of the scatter plot data, where contour levels are defined by fractions of the maximum histogram value. For instance, the green contour represents the convex hull of the points within the histogram bins that had histogram bin values greater than at least 35% of the maximum histogram value.

$q_{e,\parallel}$ also required the existence of stable solutions for all three electron components (see Appendix B for details). There are 10,983 VDFs that satisfy these criteria.

Figure 6 shows a scatter plot of $q_{e,\parallel}/q_{eo}$ versus $\beta_{ec,\parallel}$ for selection criteria *Criteria AT*. The color-coded contours indicate the regions of the highest density of points in the scatter plot. The legend in upper right corner indicates roughly the approximate fraction of points within in each contour, e.g., the fraction within the cyan contour is ~80% of the total 10,983 points shown.

The one-variable statistics for $q_{e,\parallel}$ and $q_{e,\parallel}/q_{eo}$ are shown as $X_{25\%}$–$X_{75\%}$ $(\bar{X})[\tilde{X}]$ and given by

1. $q_{e,\parallel} \sim$ 2.39–7.51(6.00)[4.11] μW m^{-2}
2. $q_{e,\parallel}/q_{eo} \sim$ 2.56–12.3(9.33)[5.84]%.

The normalized magnitudes and $\beta_{ec,\parallel}{}^{-1}$ trend are consistent with previous results (e.g., Bale et al. 2013; Wilson et al. 2013b; Lacombe et al. 2014; Tong et al. 2018, 2019a, 2019b). However, it is worth noting that the $\beta_{ec,\parallel}{}^{-1}$ trend in the $q_{e,\parallel}/q_{eo}$ may result from the fact that $q_{eo} \propto B_o{}^2 V_{Tec,\parallel} \beta_{ec,\parallel}$, that is, q_{eo} can be written in terms of $\beta_{ec,\parallel}$. Although it is beyond the scope of this work, the electron heat flux is a known source of free energy for several wave modes, and of the 10,983 VDFs with heat flux values, nearly 90% were found to be unstable to the whistler heat flux instability (e.g., Gary et al. 1994, 1999). This will be examined in more detail in Paper III.

6. Summary of Upstream Statistics

Recall that the primary purpose of this second of three parts is to provide a statistical baseline for reference of the velocity moment values under different conditions. One of the benefits of this large data set is that the *Criteria UP* results offer a useful baseline for comparison with quiescent solar wind studies. Further, in the process of the literature review, a dearth of velocity moment results for the beam/strahl component were

found (see, e.g., Appendix D). Therefore, the *Criteria UP* results can be referenced as approximate values for the solar wind.[18]

From the parameter lists and tables in Appendix C (and results in Paper I), one can see that the *Criteria UP* values, reported as $\tilde{X}\ ^{X_{75\%}}_{X_{25\%}}$, for the electron component velocity moment parameters[19] are

- *Core*
  - $n_{ec} \sim 8.29\ ^{12.6}_{4.35}\ \mathrm{cm}^{-3}$;
  - $T_{ec,tot} \sim 13.0\ ^{15.5}_{10.9}\ \mathrm{eV}$;
  - $\beta_{ec,tot} \sim 1.21\ ^{2.34}_{0.59}$;
  - $\mathcal{A}_{ec} \sim 0.98\ ^{1.00}_{0.91}$;
  - $|V_{oec,\|}| \sim 25.0\ ^{40.0}_{11.4}\ \mathrm{km\ s}^{-1}$;
  - $\kappa_{ec} \sim 7.92\ ^{10.1}_{5.44}$;
  - $s_{ec} \sim 2.00\ ^{2.03}_{2.00}$;
- *Halo*
  - $n_{eh} \sim 0.27\ ^{0.49}_{0.17}\ \mathrm{cm}^{-3}$;
  - $T_{eh,tot} \sim 47.2\ ^{55.7}_{36.3}\ \mathrm{eV}$;
  - $\beta_{eh,tot} \sim 0.17\ ^{0.32}_{0.08}$;
  - $\mathcal{A}_{eh} \sim 1.03\ ^{1.12}_{0.95}$;
  - $|V_{oeh,\|}| \sim 940\ ^{1647}_{401}\ \mathrm{km\ s}^{-1}$;
  - $\kappa_{eh} \sim 4.10\ ^{4.83}_{3.25}$;
- *Beam/Strahl*
  - $n_{eb} \sim 0.16\ ^{0.28}_{0.10}\ \mathrm{cm}^{-3}$;
  - $T_{eb,tot} \sim 38.8\ ^{46.6}_{32.4}\ \mathrm{eV}$;
  - $\beta_{eb,tot} \sim 0.09\ ^{0.16}_{0.05}$;
  - $\mathcal{A}_{eb} \sim 0.90\ ^{1.07}_{0.75}$;
  - $|V_{oeb,\|}| \sim 2110\ ^{3000}_{1400}\ \mathrm{km\ s}^{-1}$;
  - $\kappa_{eb} \sim 3.84\ ^{4.67}_{3.26}$;
- *Other*
  - $n_{eff} \sim 8.63\ ^{13.7}_{4.76}\ \mathrm{cm}^{-3}$;
  - $T_{eff,tot} \sim 14.6\ ^{17.9}_{12.5}\ \mathrm{eV}$;
  - $\beta_{eff,tot} \sim 1.42\ ^{2.63}_{0.76}$;
  - $\mathcal{A}_{eff} \sim 0.97\ ^{1.00}_{0.92}$;
  - $n_{eh}/n_{ec} \sim 3.8\ ^{7.4}_{2.2}\%$;
  - $n_{eb}/n_{ec} \sim 2.8\ ^{4.3}_{1.2}\%$;
  - $n_{eb}/n_{eh} \sim 69.3\ ^{113}_{31.2}\%$;
  - $\mathcal{T}^{eh}_{ec\,tot} \sim 3.54\ ^{4.59}_{2.69}$;
  - $\mathcal{T}^{eb}_{ec\,tot} \sim 2.87\ ^{3.59}_{2.45}$;
  - $\mathcal{T}^{eb}_{eh\,tot} \sim 0.81\ ^{1.12}_{0.62}$;
  - $\mathcal{T}^{eh}_{eff\,tot} \sim 3.07\ ^{3.98}_{2.33}$;
  - $\mathcal{T}^{eb}_{eff\,tot} \sim 2.46\ ^{3.05}_{2.14}$;
  - $\nu_{ehc} \sim (2.31\ ^{3.85}_{1.09}) \times 10^{-6}\#\ \mathrm{s}^{-1}$;
  - $\nu_{ebc} \sim (2.74\ ^{5.79}_{1.43}) \times 10^{-6}\#\ \mathrm{s}^{-1}$;
  - $\nu_{ecp} \sim (3.60\ ^{5.84}_{1.91}) \times 10^{-6}\#\ \mathrm{s}^{-1}$; and
  - $\nu_{ecc} \sim (6.45\ ^{11.0}_{3.31}) \times 10^{-6}\#\ \mathrm{s}^{-1}$.

The majority of the literature on the strahl electrons focuses entirely on the pitch-angle width versus energy and/or radial distance from the Sun (e.g., Pagel et al. 2007; Anderson et al. 2012; Gurgiolo et al. 2012; Walsh et al. 2013; Gurgiolo & Goldstein 2016; Kajdič et al. 2016), or they compute the total heat flux of the distribution (e.g., Crooker et al. 2003; Pagel et al. 2005a, 2005b; Crooker & Pagel 2008). A few studies examined density ratios among the various components (e.g., Maksimovic et al. 2005; Štverák et al. 2009; Horaites et al. 2018), and some have extrapolated an effective temperature (e.g., Tao et al. 2016a, 2016b) from a limited energy range measurement. In only one study of which the authors are aware have the beam/strahl velocity moments been presented for multiple distributions (i.e., Viñas et al. 2010). However, this study only presented results from a single, short-duration interval. Therefore, the upstream only velocity moment results for the beam/strahl component presented herein are the closest to a statistically significant presentation of those parameters in the solar wind near 1 au to date.

Note that although the *Criteria UP* values for $T_{ec,j}$ and $T_{eff,j}$ are slightly higher than those reported for the total electron temperature in a recent large, long-term statistical study of the solar wind under various conditions (e.g., Wilson et al. 2018), they are still well within the total range reported therein. The upstream values are also consistent with numerous other previous solar wind observations near 1 au (see, e.g., Appendix D). The $T_{eb,j}$ values and histograms in Tables 2 and 8 and Figure 1 are perhaps the most novel, as there have been so few studies examining the beam/strahl velocity moment parameters. In fact, the few studies that have examined the velocity moments of the beam/strahl either limited the energy range (e.g., $\geqslant$100 eV), and thus only had effective moments (e.g., Tao et al. 2016a, 2016b), or performed a limited case study (e.g., Viñas et al. 2010). The one statistical study of solar wind parameters that examined a three-component electron VDF used a truncated model function to exclude contributions from data below a cutoff energy (Štverák et al. 2009), which limited their analysis to the kappa values and number densities. Other studies focusing on the beam/strahl component discuss only the pitch-angle angular width versus energy and/or radial distance from the Sun (e.g., Anderson et al. 2012; Graham et al. 2017, 2018) or number density inferred from the pitch-angle width (e.g., Horaites et al. 2018). While these studies are clearly important and relevant to understanding the origin of the strahl and its relation to solar wind acceleration, the angular width is difficult to translate into more commonly used parameters for modeling like number density, drift velocity, or temperature. Although the *Criteria UP* values of $T_{eb,j}$ have a large range spanning from ~12 to ~280 eV, the majority fall in the more modest range of ~29–50 eV, consistent with the few previous studies that examined the beam/strahl temperature.

Again, the beam/strahl-dependent density *Criteria UP* values are novel in that there is little previous work on this topic (e.g., Maksimovic et al. 2005; Štverák et al. 2009). The values of n_{eb} are relatively unaffected by the shock in that there is little to no change in the one-variable statistics between *Criteria UP* and *Criteria DN* values. It is likely that the beam/strahl electrons are less susceptible to the effects of the shock, or they stream so quickly that there is little connection between those observed upstream and those downstream, other than the influence of shock-reflected electrons in the upstream. The beam/strahl drifts from Paper I easily exceed almost all IP shock speeds, so it is unlikely that beam/strahl electrons starting downstream could not overtake an IP shock. It is just as unlikely that beam/strahl electrons starting upstream could not outrun an IP shock. Therefore, the most likely conclusion is that only a narrow

[18] This should emphasize that in the absence of a better data set, the upstream-only results presented herein are the only statistically significant set of beam/strahl velocity moments (of which the authors are aware).

[19] The values of $|V_{os,\|}|$ exclude magnitudes below 1 km s^{-1} prior to calculating the one-variable statistics.

region near the shock ramp would exhibit shock-parameter-dependent effects on the beam/strahl fit results. This will be investigated in detail in Paper III.

The electron plasma beta *Criteria UP* values for $\beta_{ec,j}$ and $\beta_{eff,j}$ are consistent with a recent large, long-term statistical study of the solar wind under various conditions (e.g., Wilson et al. 2018) and numerous other previous solar wind observations near 1 au (e.g., Bale et al. 2013; Adrian et al. 2016). Although the $\beta_{ec,j}$ and $\beta_{eff,j}$ *Criteria UP* values have maxima in excess of 800 and 950, respectively, at least ∼75% fall below ∼2.4 and ∼2.7, respectively. That is, the upstream-only core and effective electron betas are typically consistent with low beta plasmas relative to, e.g., the intracluster medium, where $\beta_e \sim 100$ (e.g., Roberg-Clark et al. 2016, 2018). Similarly, $\beta_{eh,j}$ and $\beta_{eb,j}$ both tend to fall below ∼3.2 and ∼1.8, respectively. Further, the variation between any two components of $\beta_{eh,j}$ for any one-variable statistics value is remarkably small, with all except X_{min} falling within a few percent of each other. The differences for $\beta_{eb,j}$ show slightly more variation but are still small. Note that there is only one study (i.e., Viñas et al. 2010) of which the authors are aware that quantified $\beta_{eb,j}$, and our *Criteria UP* values are consistent with those previous results.

Similar to other velocity moments discussed above, there are no direct comparisons, of which the authors are aware, of the beam/strahl temperatures with the core or halo individually. However, the *Criteria UP* $\mathcal{T}^{eh}_{ec\,j}$ values are consistent with previous results in the solar wind (Feldman et al. 1975; Skoug et al. 2000) and near IP shocks (Wilson et al. 2009, 2012).

The range between the 5th and 95th percentiles for the $\mathcal{A}_s$ *Criteria UP* values is smallest for the core and effective anisotropies, and this holds even when examining the range between the quartiles. All $\bar{X}$ values satisfying *Criteria UP* fall within ∼6% of unity and all $\tilde{X}$ within ∼4% of unity. This can be seen in Figure 5 in that the core and halo components are sharply peaked near unity while the beam/strahl exhibits a broader distribution but still peaked near unity.

7. Discussion

The statistical analysis of 15,210 electron VDFs observed by the *Wind* spacecraft within ±2 hr of 52 IP shocks is presented. Tables of one-variable statistics combined with histograms separated by the seven selection criteria used herein provide a comprehensive summary of the properties of the electron VDFs in and around IP shocks near 1 au. The fit results satisfying the *Criteria UP* criteria are the only currently available data set of beam/strahl velocity moment values near 1 au. The net electron heat flux and the two-particle collision rates between all electron components and protons and alpha-particles are also provided.

From Tables 2–7 (and results in Paper I) one can see that the *Criteria AT* values, reported as $\tilde{X}\,{}^{X_{75\%}}_{X_{25\%}}$, for the electron component velocity moment parameters[20] are

- *Core*
  - $n_{ec} \sim 11.3\,{}^{19.4}_{6.55}\,\mathrm{cm^{-3}}$;
  - $T_{ec,tot} \sim 14.6\,{}^{18.6}_{12.0}\,\mathrm{eV}$;
  - $\beta_{ec,tot} \sim 0.93\,{}^{2.01}_{0.52}$;
  - $\mathcal{A}_{ec} \sim 0.98\,{}^{1.01}_{0.90}$;
  - $|V_{oec,\|}| \sim 29.1\,{}^{49.7}_{14.2}\,\mathrm{km\ s^{-1}}$;
  - $\kappa_{ec} \sim 7.92\,{}^{10.1}_{5.44}$;
  - $s_{ec} \sim 2.00\,{}^{2.04}_{2.00}$;
  - $p_{ec} \sim 3.00\,{}^{4.00}_{2.20}$;
  - $q_{ec} \sim 2.00\,{}^{2.38}_{2.00}$;
- *Halo*
  - $n_{eh} \sim 0.36\,{}^{0.63}_{0.20}\,\mathrm{cm^{-3}}$;
  - $T_{eh,tot} \sim 48.4\,{}^{58.1}_{37.4}\,\mathrm{eV}$;
  - $\beta_{eh,tot} \sim 0.11\,{}^{0.22}_{0.05}$;
  - $\mathcal{A}_{eh} \sim 1.03\,{}^{1.12}_{0.95}$;
  - $|V_{oeh,\|}| \sim 901\,{}^{1692}_{362}\,\mathrm{km\ s^{-1}}$;
  - $\kappa_{eh} \sim 4.37\,{}^{5.31}_{3.57}$;
- *Beam/Strahl*
  - $n_{eb} \sim 0.17\,{}^{0.29}_{0.10}\,\mathrm{cm^{-3}}$;
  - $T_{eb,tot} \sim 40.2\,{}^{50.0}_{33.7}\,\mathrm{eV}$;
  - $\beta_{eb,tot} \sim 0.05\,{}^{0.10}_{0.02}$;
  - $\mathcal{A}_{eb} \sim 0.93\,{}^{1.11}_{0.78}$;
  - $|V_{oeb,\|}| \sim 2282\,{}^{3000}_{1400}\,\mathrm{km\ s^{-1}}$;
  - $\kappa_{eb} \sim 4.17\,{}^{5.11}_{3.41}$;
- *Other*
  - $n_{eff} \sim 11.9\,{}^{20.3}_{6.92}\,\mathrm{cm^{-3}}$;
  - $T_{eff,tot} \sim 16.0\,{}^{20.5}_{13.6}\,\mathrm{eV}$;
  - $\beta_{eff,tot} \sim 1.06\,{}^{2.26}_{0.63}$;
  - $\mathcal{A}_{eff} \sim 0.97\,{}^{1.01}_{0.91}$;
  - $n_{eh}/n_{ec} \sim 3.2\,{}^{6.1}_{1.8}\%$;
  - $n_{eb}/n_{ec} \sim 1.8\,{}^{3.6}_{0.7}\%$;
  - $n_{eb}/n_{eh} \sim 50.0\,{}^{96.2}_{24.4}\%$;
  - $\mathcal{T}^{eh}_{ec\,tot} \sim 3.19\,{}^{4.04}_{2.39}$;
  - $\mathcal{T}^{eb}_{ec\,tot} \sim 2.73\,{}^{3.35}_{2.22}$;
  - $\mathcal{T}^{eb}_{eh\,tot} \sim 0.85\,{}^{1.14}_{0.66}$;
  - $\mathcal{T}^{eh}_{eff\,tot} \sim 2.88\,{}^{3.64}_{2.17}$;
  - $\mathcal{T}^{eb}_{eff\,tot} \sim 2.44\,{}^{3.03}_{1.99}$;
  - $\nu_{ehc} \sim (2.90\,{}^{4.61}_{1.30}) \times 10^{-6}\#\ \mathrm{s^{-1}}$;
  - $\nu_{ebc} \sim (3.60\,{}^{6.45}_{1.78}) \times 10^{-6}\#\ \mathrm{s^{-1}}$;
  - $\nu_{ecp} \sim (4.36\,{}^{7.07}_{1.93}) \times 10^{-6}\#\ \mathrm{s^{-1}}$; and
  - $\nu_{ecc} \sim (7.93\,{}^{12.9}_{3.69}) \times 10^{-6}\#\ \mathrm{s^{-1}}$.

Although the detailed analysis of the electron VDF fit parameters on the macroscopic shock properties is beyond the scope of this work and included in Paper III, some statistical dependencies are discussed herein. The dependencies of $T_{s,j}$ and n_{es} on the selection criteria are weak for the halo and beam/strahl but clear for the core and consistent with expectations. That is, the core is heated and compressed in the downstream compared to the upstream.

Although the individual $T_{s,j}$ did not show significant variations between the selection criteria, the $\mathcal{T}^{s'}_{s\,j}$ did show some strong dependencies on the selection criteria. The core-dependent ratios (i.e., $s = c$) show some rather dramatic differences in the histogram profiles even though the primary peaks are relatively constant (except for *Criteria HM* shocks). In contrast, the $\mathcal{T}^{eb}_{eh\,j}$ histograms are much stabler in profile and one-variable statistics values between any two opposing selection criteria. There are still differences in the histograms of *Criteria PA* and *Criteria HM* shocks, but they are subtler than those for either of the core-dependent ratios.

The $\mathcal{A}_{ec}$ histograms are primarily different in the lower-value tails between any two opposing selection criteria. For instance,

[20] The values of $|V_{os,\|}|$ exclude magnitudes below 1 km s^{-1} prior to calculating the one-variable statistics.

the histograms are tripolar for *Criteria PA* and *Criteria HM* shocks, but only bipolar for *Criteria LM* shocks and effectively monopolar for *Criteria PE* shocks. Note that the $\mathcal{A}_{ec}$ values do not deviate to values much larger than unity, i.e., the core is more often oblate in the parallel than perpendicular directions. In contrast, the $\mathcal{A}_{eh}$ histograms are monopolar and peaked near unity with large tails on both sides of unity, i.e., the halo can be oblate in both the parallel and perpendicular directions but tends toward near isotropy. Finally, the $\mathcal{A}_{eb}$ show an even broader range of values, and only the *Criteria PA* values show a bipolar distribution. The primary peak for all selection criteria is near ∼0.9 except for *Criteria HM*, which is closer to unity. Although the $\mathcal{A}_{eb}$ histograms have long tails on both sides of the primary peaks, the distributions are skewed toward smaller values.

Lastly, the $\beta_{s,j}$ values showed dramatic differences between opposing selection criteria with one-variable statistic values differing by upward of 100%. Not only do the peaks change between opposing selection criteria, but the histogram profiles show remarkable differences as well. The core beta values are stabler than either the halo or beam/strahl, but even the core shows significant differences. Thus, the electron component betas seem to exhibit the most striking dependencies on macroscopic shock parameters.

The fit results were also used to calculate the two-particle Coulomb collision rates, all of which had median values below 8×10^{-6} # s^{-1}, or less than ∼5 collisions per week (for *Criteria AT*). When calculating the collisional mean free paths, the only two-particle collision rates with median values less than one astronomical unit are for proton–proton collisions. Next, the alpha-alpha and core-core values are <2 au, followed by beam-core, proton-alpha, and halo-core satisfying <8 au. The rest of the median values all satisfy >15 au. That is, the median distance before a collision occurs for most species is nearly the orbital radius of Uranus. The bottom five (or largest five) median mean free paths all satisfy >185 au. That is, the median location before experiencing a collision is outside the heliosphere for the most tenuous of the species examined herein, i.e., alpha-particles, halo, and beam/strahl electrons. Yet despite the low particle–particle collision rates, most of the core exponents (i.e., ∼80.5%) satisfy $2.00 \leqslant s_{ec} \leqslant 2.05$, which are self-similar VDFs that are visually indistinguishable from Maxwellians (see Paper I for details). This seems to suggest some remnant property of the solar atmosphere where collision rates are much higher (e.g., Marsch 2006; Kasper et al. 2017; Kasper & Klein 2019).

The parallel electron heat flux was also calculated for VDFs with stable solutions for all three electron components. The magnitudes and normalized values had the following ranges: $q_{e,\parallel} \sim 10^{-6}$–76 $\mu W\,m^{-2}$ and $q_{e,\parallel}/q_{eo} \sim 10^{-5}$–190%. However, 95% of the magnitudes and normalized values satisfied $\leqslant$16.2 $\mu W\,m^{-2}$ and $\leqslant$24.4%, respectively, consistent with previous work (e.g., Bale et al. 2013; Wilson et al. 2013b; Lacombe et al. 2014; Tong et al. 2018, 2019a, 2019b). A preliminary examination found that as many as ∼90% of the observed electron VDFs are unstable to the whistler heat flux instability (e.g., Gary et al. 1994, 1999); however, instability analysis is beyond the scope of this work and will be discussed in Paper III.

The results presented herein provide a statistically significant list of values and histogram distributions for reference and baselines in future work. Given the large statistics in this investigation, the beam/strahl fits for selection criteria *Criteria UP* are now the most comprehensive attempt to parameterize the beam/strahl electron velocity moments in the ambient solar wind. These results are useful for multiple modeling and simulation studies in addition to comparison with inaccessible regions like the intracluster medium. Further, these results will provide a statistical baseline for the *Parker Solar Probe* mission and the future *Solar Orbiter* and *IMAP* missions.

The authors thank A. F. Viñas and D. A. Roberts for useful discussions of basic plasma physics and C. Markwardt for helpful feedback on the usage nuances of his MPFIT software. The work was supported by the International Space Science Institute's (ISSI) International Teams programme. L.B.W. was partially supported by *Wind* MO&DA grants and a Heliophysics Innovation Fund (HIF) grant. L.-J.C. and S.W. were partially supported by the *MMS* mission in addition to NASA grants 80NSSC18K1369 and 80NSSC17K0012, NSF grants AGS-1619584 and AGS-1552142, and DOE grant DESC00 16278. D.L.T. was partially supported by NASA grant NNX16 AQ50G. M.L.S. was partially supported by grants NNX14AT 26G and NNX13AI75G. J.C.K. was partially supported by NASA grants NNX14AR78G and 80NSSC18K0986. D.C. was partially supported by grants NNX17AG30G, GO8-19110A, 80NSSC18K1726, 80NSSC18K1218, and NSF grant 1714658. S.J.S. was partially supported by the *MMS*/FIELDS investigation. C.S.S. was partially supported by NASA grant NNX16 AI59G and NSF SHINE grant 1622498. S.D.B. and C.S.S. were partially supported by NASA grant NNX16AP95G. S.D. B. acknowledges the support of the Leverhulme Trust Visiting Professor program. M.P.P. and K.A.G. were supported by *Parker Solar Probe* instrument funds.

Appendix A
Definitions and Notation

As in Paper I, in this appendix the symbols and notation used throughout will be defined. For all direction-dependent parameters we use the subscript j to represent the direction, where $j = tot$ for the entire distribution, $j = \parallel$ for the the parallel direction, and $j = \perp$ for the perpendicular direction, where parallel/perpendicular is with respect to the quasi-static magnetic field vector, $\boldsymbol{B}_o$ (nT). The generic subscript s is used to denote the particle species (e.g., electrons, protons, etc.) or the component of a single particle species (e.g., electron core). For the electron components, the subscript will be $s = ec$ for the core, $s = eh$ for the halo, $s = eb$ for the beam/strahl, $s = eff$ for the effective, and $s = e$ for the total/entire population. Below are the symbol/parameter definitions:

- *one-variable statistics*
  - $X_{min} \equiv$ minimum
  - $X_{max} \equiv$ maximum
  - $\bar{X} \equiv$ mean
  - $\tilde{X} \equiv$ median
  - $X_{25\%} \equiv$ lower quartile
  - $X_{75\%} \equiv$ upper quartile
  - $\sigma \equiv$ standard deviation
  - $\sigma^2 \equiv$ variance
- *fundamental parameters*
  - $\varepsilon_o \equiv$ permittivity of free space
  - $\mu_o \equiv$ permeability of free space

- $c \equiv$ speed of light in vacuum (km s^{-1}) $= (\varepsilon_o\ \mu_o)^{-1/2}$
- $k_B \equiv$ the Boltzmann constant (J K^{-1})
- $e \equiv$ the fundamental charge (C)

– *plasma parameters*

- $n_s \equiv$ the number density (cm^{-3}) of species s
- $m_s \equiv$ the mass (kg) of species s
- $Z_s \equiv$ the charge state of species s
- $q_s \equiv$ the charge (C) of species $s = Z_s\ e$
- $T_{s,j} \equiv$ the scalar temperature (eV) of the jth component of species s
- $\mathcal{T}_{j_s}^{s'} = (T_{s'}/T_s)_j \equiv$ the temperature ratio (N/A) of species s and s' of the jth component
- $\mathcal{A}_s = (T_\perp/T_\parallel)_s \equiv$ the temperature anisotropy (N/A) of species s
- $V_{Ts,j} \equiv$ the most probable thermal speed (km s^{-1}) of a one-dimensional velocity distribution (see Equation 1(c))
- $\boldsymbol{V}_{os} \equiv$ the drift velocity (km s^{-1}) of species s in the plasma bulk flow rest frame
- $C_s \equiv$ the sound or ion-acoustic sound speed (km s^{-1}) (see supplemental PDF file in Wilson et al. 2019b, for definitions)
- $V_A \equiv$ the Alfvén speed (km s^{-1}) (see supplemental PDF file in Wilson et al. 2019b, for definitions)
- $V_f \equiv$ the fast mode speed (km s^{-1}) (see supplemental PDF file in Wilson et al. 2019b, for definitions)
- $\Omega_{cs} \equiv$ the angular cyclotron frequency (rad s^{-1}) (see Equation 1(d))
- $\omega_{ps} \equiv$ the angular plasma frequency (rad s^{-1}) (see Equation 1(e))
- $\lambda_{De} \equiv$ the electron Debye length (m) (see Equation 1(f))
- $\rho_{cs} \equiv$ the thermal gyroradius (km) (see Equation 1(g))
- $\lambda_s \equiv$ the inertial length (km) (see Equation 1(h))
- $\beta_{s,j} \equiv$ the plasma beta (N/A) of the jth component of species s (see Equations 1(i) and (j))
- $\kappa_s \equiv$ the kappa exponent of species s (see, e.g., Wilson et al. 2019a, for definition in model fit equation)
- $s_s \equiv$ the symmetric self-similar exponent of species s (see, e.g., Wilson et al. 2019a, for definition in model fit equation)
- $p_s(q_s) \equiv$ the parallel(perpendicular) asymmetric self-similar exponent of species s (see, e.g., Wilson et al. 2019a, for definition in model fit equation)
- $\phi_{sc} \equiv$ the scalar, quasi-static spacecraft potential (eV) (e.g., Scime et al. 1994; Pulupa et al. 2014) (see Appendices of Paper I for more details)
- $E_{min} \equiv$ the minimum energy bin midpoint value (eV) of an electrostatic analyzer (see, e.g., Appendices in Wilson et al. 2017, 2018)
- $q_{e,\parallel} = \frac{m_e}{2} \int d^3v\ f_e^{(mod)} v_\parallel\ v^2 \equiv$ the parallel electron heat flux (μW m^{-2}) of the entire electron VDF model, $f_e^{(mod)} = f^{(core)} + f^{(halo)} + f^{(beam)}$
- $q_{eo} = \frac{3}{2}\ m_e\ n_e\ V_{Tec,\parallel}^3 \equiv$ the free-streaming limit electron heat flux (μW m^{-2}) (e.g., Gary et al. 1999).

Similar to Paper I, the variables that rely on multiple parameters are given in the following equations:

$$T_{eff,j} = \frac{\sum_s n_s\ T_{s,j}}{\sum_s n_s} \tag{1a}$$

$$T_{s,tot} = \frac{1}{3}(T_{s,\parallel} + 2\ T_{s,\perp}) \tag{1b}$$

$$V_{Ts,j} = \sqrt{\frac{2\ k_B\ T_{s,j}}{m_s}} \tag{1c}$$

$$\Omega_{cs} = \frac{q_s\ B_o}{m_s} \tag{1d}$$

$$\omega_{ps} = \sqrt{\frac{n_s\ q_s^2}{\varepsilon_o\ m_s}} \tag{1e}$$

$$\lambda_{De} = \frac{V_{Te,tot}}{\sqrt{2}\ \omega_{pe}} = \sqrt{\frac{\varepsilon_o\ k_B\ T_{e,tot}}{n_e\ e^2}} \tag{1f}$$

$$\rho_{cs} = \frac{V_{Ts,tot}}{\Omega_{cs}} \tag{1g}$$

$$\lambda_s = \frac{c}{\omega_{ps}} \tag{1h}$$

$$\beta_{s,j} = \frac{2\mu_o n_s k_B T_{s,j}}{|\boldsymbol{B}_o|^2} \tag{1i}$$

$$\beta_{eff,j} = \frac{2\mu_o n_{eff} k_B T_{eff,j}}{|\boldsymbol{B}_o|^2}, \tag{1j}$$

where n_{eff} is defined as

$$n_{eff} = \sum_s n_{es}. \tag{1k}$$

Following the format from Wilson et al. (2018), one can calculate estimates of Coulomb collision rates[21] (e.g., Spitzer & Härm 1953; Krall & Trivelpiece 1973; Schunk 1975, 1977; Hinton 1984; Hernandez & Marsch 1985), $\nu_{ss'}$, between species s and s' given by

$$\nu_{ss'} = \frac{C_{ss'}\ n_{s'}}{V_{Tss'}^3}\ \ln \Lambda_{ss'} \tag{2a}$$

$$C_{ss'} = \frac{A_{ss'}\ e^4}{3(4\pi\varepsilon_o)^2\ \mu_{ss'}^2} \tag{2b}$$

$$\Lambda_{ss'} \simeq \frac{(4\pi\varepsilon_o)\ \mu_{ss'}\ V_{Tss'}^2}{\sqrt{2}\ Z_s\ Z_{s'}\ e^2} \times \left[\left(\frac{\omega_{ps}}{V_{Ts,tot}}\right)^2 + \left(\frac{\omega_{ps'}}{V_{Ts',tot}}\right)^2\right]^{-1/2} \tag{2c}$$

$$V_{Tss'} = \sqrt{V_{Ts,tot}^2 + V_{Ts',tot}^2} \tag{2d}$$

$$\mu_{ss'} = \frac{m_s\ m_{s'}}{(m_s + m_{s'})}, \tag{2e}$$

where the species-dependent integration constants $A_{ss'}$ are given by

$$A_{ee} = 4\sqrt{2\pi} \tag{3a}$$

$$A_{pp} = 4\sqrt{2\pi} \tag{3b}$$

$$A_{\alpha\alpha} = 64\sqrt{2\pi} \tag{3c}$$

$$A_{ep} = 2\sqrt{4\pi} \tag{3d}$$

$$A_{e\alpha} = 8\sqrt{4\pi} \tag{3e}$$

$$A_{p\alpha} = 8\sqrt{2\pi}. \tag{3f}$$

[21] Note that the rates are for isotropic Maxwellian velocity distributions and would change for kappa and self-similar depending on the exponent values (e.g., Marsch & Livi 1985).

Then, the particle rms mean free path is given by

$$\lambda_{ss'}{}^{\rm mpf} = \frac{V_{Tss'}}{\nu_{ss'}}. \quad (4)$$

For the macroscopic shock parameters, the values are averaged over asymptotic regions away from the shock transition region.

- *shock parameters*
  - subscripts up and dn ≡ denote the upstream (i.e., before the shock arrives timewise at the spacecraft for a forward shock) and downstream (i.e., the shocked region)
  - $\langle Q \rangle_j \equiv$ the average of parameter Q over the jth shock region, where $j =$ up or dn
  - $\Delta Q = \langle Q \rangle_{\rm dn} - \langle Q \rangle_{\rm up} \equiv$ the change in the asymptotic average of parameter Q over the jth shock region
  - $\mathcal{R}_{ns} = \langle n_s \rangle_{\rm dn} / \langle n_s \rangle_{\rm up} \equiv$ the shock compression ratio of species s
  - $\mathcal{R}_{Ts,j} = \langle T_{s,j} \rangle_{\rm dn} / \langle T_{s,j} \rangle_{\rm up} \equiv$ the downstream-to-upstream jth component temperature ratio of species s
  - $\boldsymbol{n}_{\rm sh} \equiv$ the shock normal unit vector (N/A)
  - $\theta_{\rm Bn} \equiv$ the shock normal angle[22] (deg)
  - $\langle |V_{\rm shn}| \rangle_j \equiv$ the jth region average shock normal speed (km s^{-1}) in the spacecraft frame
  - $\langle |U_{\rm shn}| \rangle_j \equiv$ the jth region average shock normal speed (km s^{-1}) in the shock rest frame (i.e., the speed of the flow relative to the shock)
  - $\langle M_{\rm A} \rangle_j \equiv$ the jth region average Alfvénic Mach number (N/A) $= \langle |U_{\rm shn}| \rangle_j / \langle V_{\rm A} \rangle_j$
  - $\langle M_f \rangle_j \equiv$ the jth region average fast mode Mach number (N/A) $= \langle |U_{\rm shn}| \rangle_j / \langle V_f \rangle_j$
  - $M_{\rm cr} \equiv$ the first critical Mach number (N/A)

These definitions are used throughout.

Appendix B
Integrated Velocity Moments

This appendix provides details regarding the numerical integration of the total model fit VDFs to determine velocity moments and comparison with summed velocity moments. Note that velocity moments of the components can be summed to find totals for the entire VDF against which one can compare an integrated equivalent. The comparison is performed as a sanity check.

The nth moment of a VDF, $f(\boldsymbol{x}, \boldsymbol{v}, t)$, is generically defined as the expectation value of the nth order of a dynamical function, $g(\boldsymbol{x}, \boldsymbol{v})$, given by

$$\langle g^n(\boldsymbol{x}, \boldsymbol{v}) \rangle \equiv \int d^3v \; g^n(\boldsymbol{x}, \boldsymbol{v}) \, f(\boldsymbol{x}, \boldsymbol{v}, t), \quad (5)$$

where the zeroth moment is the volume density (e.g., number density), the first relates to the peak of the distribution (e.g., the bulk flow velocity), the second to the width of the peak (e.g., random kinetic energy density or pressure tensor), the third to the skewness (e.g., heat flux tensor), the fourth to the kurtosis, etc.

For velocity moment calculations of in situ spacecraft measurements, the dynamical function is the velocity coordinate $\boldsymbol{v}$ and the spatial and temporal dependence drop out, resulting in $f(\boldsymbol{x}, \boldsymbol{v}, t) \rightarrow f(\boldsymbol{v})$ for each VDF observed.[23] The total/entire electron model VDF, $f_s{}^{(\rm mod)} = f^{(\rm core)} + f^{(\rm halo)} + f^{(\rm beam)}$, is constructed from the valid fit parameters discussed in Section 2 only for VDFs with stable solutions for all three components. The integrals are calculated in the core electron rest frame; thus, the only relevant heat flux component is the parallel, $q_{e,\parallel}$, because the suprathermal electrons have no finite perpendicular drift velocities (see, e.g., Paper I).

The integrals are numerically approximated using the Simpson's $\frac{1}{3}$ Rule algorithm. Since the models are gyrotropic, the two perpendicular velocities are symmetric, reducing the three-dimensional integrals to two-dimensional integrals.[24] Some simple benchmarking tests revealed that the range of the regular velocity grid coordinates was more important than the number of grid points for reducing the difference between the "known" and integrated value of any given velocity moment. It was found that the minimum threshold for grid range and density while simultaneously reducing the computational time to keep the percent difference within less than a percent was ±80,000 km s^{-1} and 301 × 301 points. The velocity grid is constructed in linear space because tests of logarithmically spaced velocity coordinates resulted in larger percent differences.

For brevity the percent difference between the summed and integrated velocity moment parameters is defined as $\Delta Q_{i2f} = |Q_{\rm int} - Q_{\rm eff}| / Q_{\rm eff} \times 100\%$, where the subscript eff is for *effective* and int is for *integrated*. For instance, the percent difference between the summed and integrated electron density is given as $\Delta n_{i2f} = |n_{\rm int} - n_{\rm eff}| / n_{\rm eff} \times 100\%$ (the e for electron is assumed, since only electron VDFs are integrated). The one-variable statistics of these percent differences are shown as $X_{25\%}$–$X_{75\%}$ ($\bar{X}$)[$\tilde{X}$] and given by the following:

1. $\Delta\, n_{i2f} \sim$ 0.001%–0.66%(0.74%)[0.002%]
2. $\Delta |\boldsymbol{V}_{{\rm oe},\parallel}|_{i2f} \sim$ 0.001%–848%(3068%)[3.14%]
3. $\Delta T_{e\parallel,i2f} \sim$ 1.21%–6.59%(4.68%)[3.04%]
4. $\Delta T_{e\perp,i2f} \sim$ 0.003%–1.94%(2.28%)[0.012%]
5. $\Delta T_{{\rm etot},i2f} \sim$ 0.74%–25.0%(26.3%)[2.47%].

The large values of the parallel drift percent difference are dominated by outliers, as evidenced by the small median value. Thus, the numerical integration results are within expected uncertainties/errors.

These tests were performed to verify the accuracy of the integrated $q_{e,\parallel}$ values since there is no properly summed value from the original fit parameter sets. Further, the inaccuracy of this type of numerical integration increases with increasing velocity moment (e.g., Song et al. 1997; Paschmann & Daly 1998; Gershman et al. 2015), hence why the errors in the lowest moments were minimized prior to calculation of the heat flux.

Appendix C
Extra Statistics

This appendix presents additions to the statistics (Figures 7–11) and (Tables 8–13) presented in the main paper. The tables are referenced as supplements for the statistics in the paper.

[22] The acute reference angle between $\langle \boldsymbol{B}_o \rangle_{\rm up}$ and $\boldsymbol{n}_{\rm sh}$.

[23] Note that the pressure and heat flux tensors should be computed in the species rest frame; thus, the dynamical function is the peculiar velocity or $\boldsymbol{v} - \boldsymbol{V}_{os}$.

[24] $d^3v \rightarrow \pi \, |v_\perp| \, dv_\perp \, dv_\parallel$.

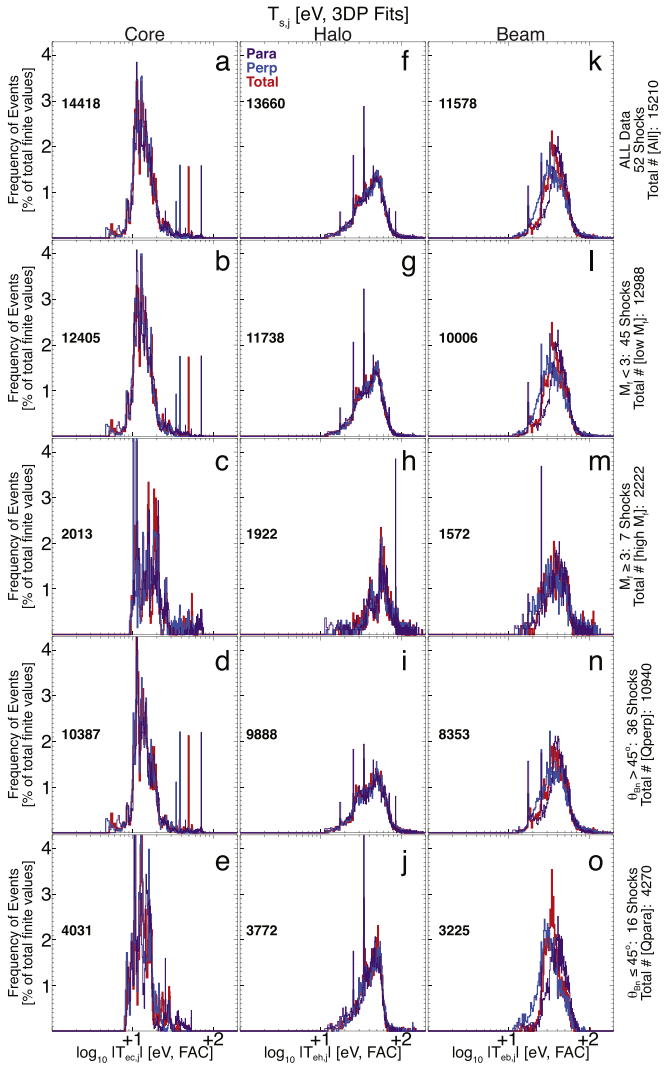

Figure 7. Temperatures (eV) for different electron components in each column with a similar format to that of Figure 1 but for other selection criteria. The first row is the same as that in Figure 1, but the next four are, in the following order, low Mach number, high Mach number, quasi-perpendicular, and quasi-parallel shocks. Similar to Figure 1, the total numbers of finite points for each panel are the same for each color-coded line (label in panel (f)). To the far right are the total number of VDFs analyzed for each criterion for reference.

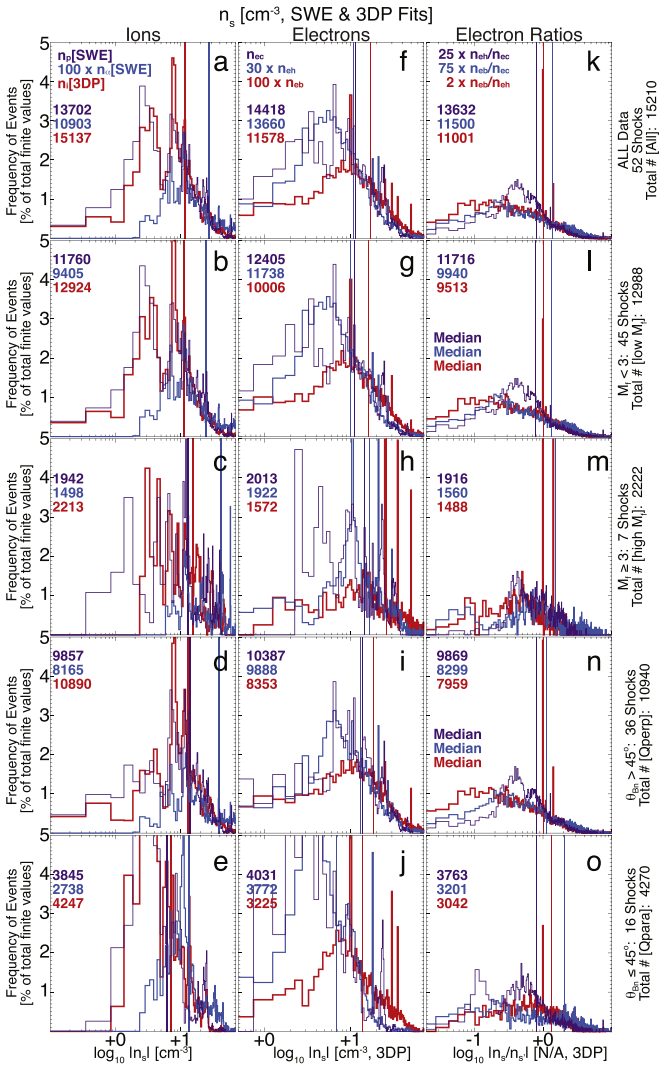

Figure 8. Densities (cm^{-3}) and density ratios with a similar format to that of Figure 2 but for other selection criteria. The top row is the same as that in Figure 2 for reference, but the next four rows are the same as in Figure 7.

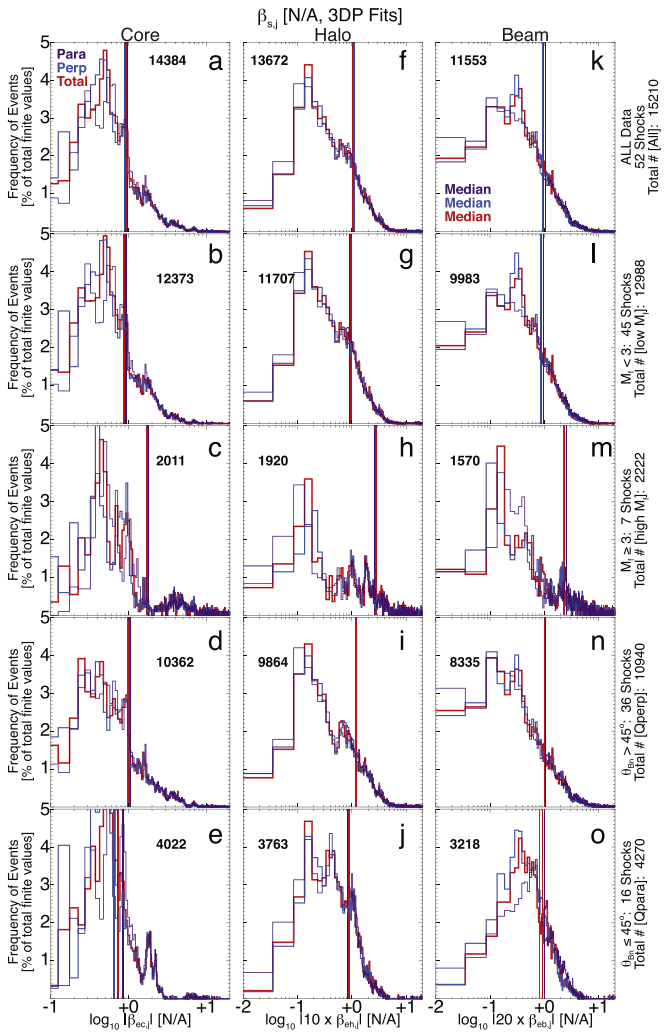

Figure 9. Same format as Figures 7 and 8, except for electron betas (N/A). Similar to Figure 3, all $\beta_{eh,j}$ and $\beta_{eb,j}$ values were offset by constant factors of 10 and 20, respectively, to reduce the horizontal axis dynamic range.

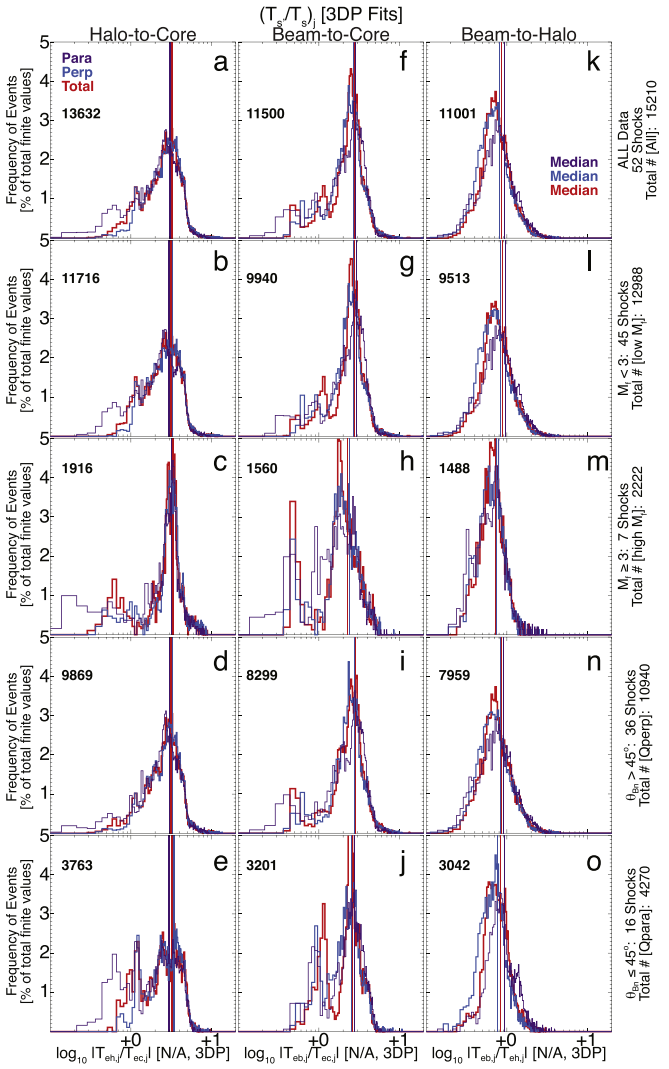

Figure 10. Same format as Figures 7 and 8, except for electron temperature ratios (N/A).

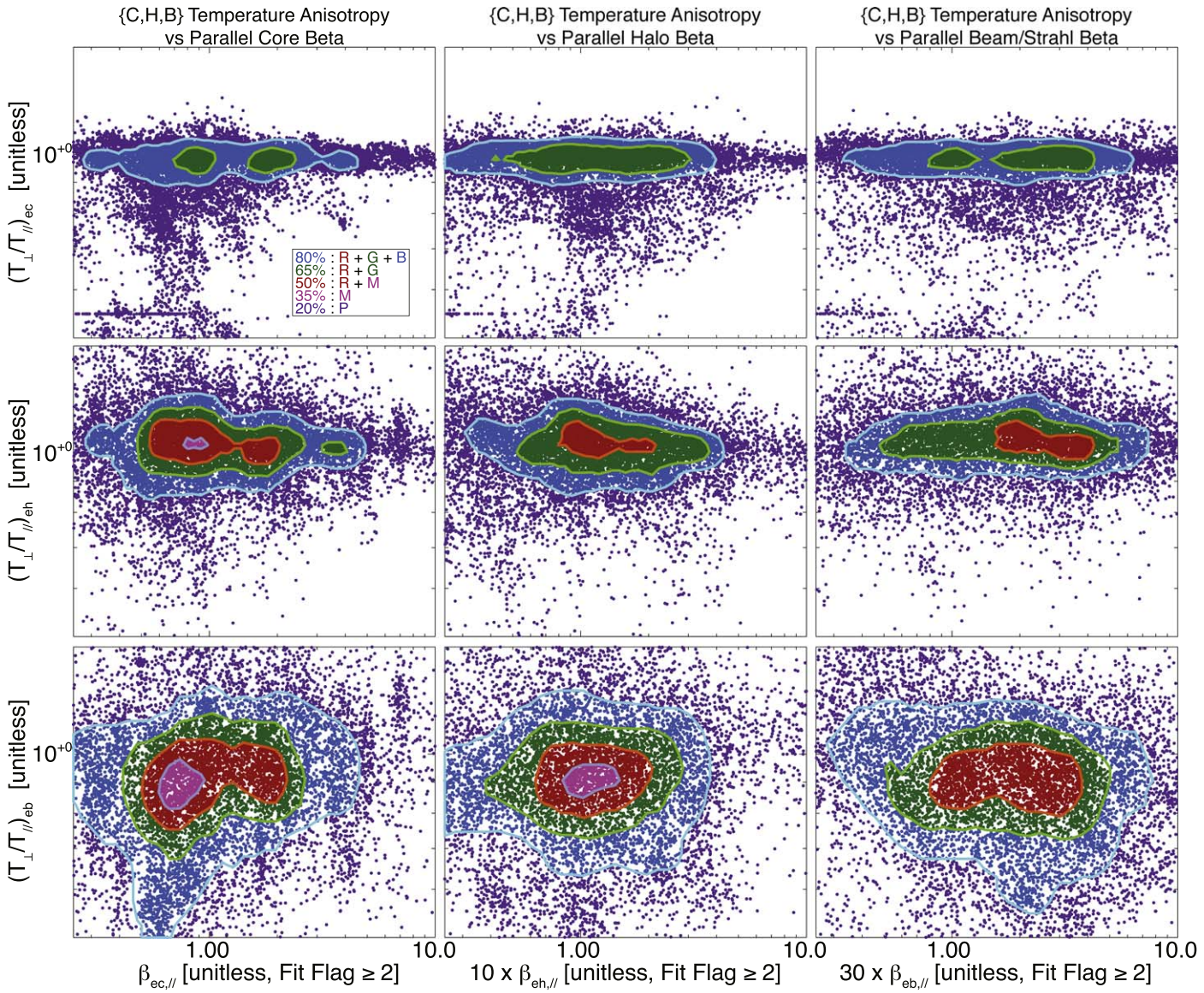

Figure 11. Temperature anisotropy, $\mathcal{A}_{es}$ (N/A), vs. parallel electron beta, $\beta_{s,\parallel}$ (N/A), of electron component *s*. The color-coded contours (legend in lower right corner of top left panel) are generated in the same fashion as those in Figure 6. Note that the halo and beam/strahl beta values have been increased by factors of 10 and 30, respectively, to maintain a uniform horizontal axis scale across all columns.

Table 8
Temperature Parameters

Temp. (eV)	$X_{\min}$ [a]	$X_{\max}$	$\bar{X}$	$\tilde{X}$	$X_{25\%}$	$X_{75\%}$	$X_{\min}$	$X_{\max}$	$\bar{X}$	$\tilde{X}$	$X_{25\%}$	$X_{75\%}$
	Criteria UP: 6546 VDFs						*Criteria DN: 8664 VDFs*					
$T_{ec,\parallel}$	5.67	36.7	14.1	13.2	11.2	16.2	7.34	89.1	22.7	16.5	13.6	24.7
$T_{ec,\perp}$	4.75	26.5	13.0	12.8	10.9	15.1	7.16	62.8	19.0	16.3	13.2	20.7
$T_{ec,tot}$	5.06	27.3	13.4	13.0	10.9	15.5	7.22	67.2	20.2	16.4	13.4	22.6
$T_{eh,\parallel}$	11.6	188	46.6	46.3	35.7	54.9	11.7	249	50.8	48.2	35.7	60.5
$T_{eh,\perp}$	11.5	204	48.5	47.5	35.7	56.9	11.4	255	52.4	49.6	38.1	60.1
$T_{eh,tot}$	11.6	180	47.9	47.2	36.3	55.7	11.7	222	51.8	49.0	38.0	59.8
$T_{eb,\parallel}$	12.1	280	43.0	42.2	36.4	49.9	11.5	201	45.1	43.6	36.0	52.4
$T_{eb,\perp}$	11.9	264	39.8	36.6	28.7	46.2	11.7	277	44.7	41.3	32.3	53.1
$T_{eb,tot}$	12.3	269	40.9	38.8	32.4	46.6	14.3	238	44.9	41.6	34.8	52.4
$T_{eff,\parallel}$	6.97	95.6	16.3	14.9	12.8	18.6	8.41	167	23.8	17.6	14.6	26.3
$T_{eff,\perp}$	4.93	111	15.1	14.4	12.3	17.3	8.17	170	20.3	17.3	14.2	22.4
$T_{eff,tot}$	5.61	106	15.5	14.6	12.5	17.9	8.35	169	21.4	17.4	14.4	24.3
	Criteria LM: 12,988 VDFs						*Criteria HM: 2222 VDFs*					
$T_{ec,\parallel}$	5.67	84.0	17.9	14.7	11.9	18.2	9.49	89.1	26.3	19.5	14.7	26.3
$T_{ec,\perp}$	4.75	56.0	15.6	14.0	11.9	17.1	9.23	62.8	22.0	18.5	14.2	25.2
$T_{ec,tot}$	5.06	61.2	16.3	14.2	11.9	17.5	9.45	67.2	23.4	19.0	14.4	25.8
$T_{eh,\parallel}$	11.7	249	46.2	45.7	34.8	55.0	11.6	221	66.2	60.6	49.8	74.7
$T_{eh,\perp}$	11.4	255	47.8	47.2	35.9	56.4	11.5	226	68.7	60.6	49.4	78.5
$T_{eh,tot}$	11.7	203	47.3	46.9	36.2	55.6	11.6	222	67.9	60.6	49.1	76.5
$T_{eb,\parallel}$	11.5	201	43.9	42.8	36.4	51.1	12.1	280	46.3	43.2	34.6	53.2
$T_{eb,\perp}$	11.7	275	41.7	38.7	30.4	49.3	11.9	277	48.4	42.8	32.1	55.4
$T_{eb,tot}$	13.8	238	42.4	39.9	33.6	49.4	12.3	269	47.7	42.9	34.1	53.0
$T_{eff,\parallel}$	6.97	78.8	19.3	16.0	13.4	20.0	11.3	167	28.5	21.8	16.6	29.7
$T_{eff,\perp}$	4.93	89.9	17.1	15.3	13.1	19.0	10.3	170	24.4	20.3	16.5	28.6
$T_{eff,tot}$	5.61	80.6	17.8	15.5	13.3	19.3	11.1	169	25.8	20.7	16.5	29.1
	Criteria PE: 10,940 VDFs						*Criteria PA: 4270 VDFs*					
$T_{ec,\parallel}$	5.67	89.1	19.3	14.9	12.1	19.1	7.93	55.8	18.5	15.2	12.2	19.1
$T_{ec,\perp}$	4.75	62.8	16.9	14.6	12.0	18.5	7.78	50.3	15.2	13.7	12.0	17.0
$T_{ec,tot}$	5.06	67.2	17.7	14.7	12.0	18.7	7.88	51.4	16.3	14.2	12.3	17.6
$T_{eh,\parallel}$	11.6	249	50.8	48.9	36.0	60.8	11.7	171	44.5	44.8	35.1	52.5
$T_{eh,\perp}$	11.4	226	52.1	49.6	37.4	61.0	11.9	255	47.2	46.8	36.9	54.9
$T_{eh,tot}$	11.6	222	51.7	49.2	37.6	60.5	12.0	203	46.3	46.4	36.8	53.5
$T_{eb,\parallel}$	11.5	280	44.5	42.8	36.4	51.6	12.1	201	43.6	42.8	35.6	51.0
$T_{eb,\perp}$	12.6	277	44.8	41.5	31.9	52.4	11.7	207	37.0	34.3	28.4	43.7
$T_{eb,tot}$	13.8	269	44.7	41.8	34.5	51.7	12.3	151	39.2	36.9	32.2	44.9
$T_{eff,\parallel}$	6.97	167	20.9	16.3	13.6	21.1	7.93	65.0	19.8	16.7	13.6	20.9
$T_{eff,\perp}$	4.93	170	18.7	15.9	13.5	20.3	8.22	66.7	16.7	15.2	13.3	18.2
$T_{eff,tot}$	5.61	169	19.4	16.1	13.6	20.6	8.13	66.0	17.7	15.6	13.6	18.7

Notes. For symbol definitions, see Appendix A.
[a] Header symbols match those of Table 2.

Table 9
Density Parameters

n_s (cm^{-3})	$X_{\min}$ [a]	$X_{\max}$	$\bar{X}$	$\tilde{X}$	$X_{25\%}$	$X_{75\%}$	$X_{\min}$	$X_{\max}$	$\bar{X}$	$\tilde{X}$	$X_{25\%}$	$X_{75\%}$
	Criteria UP: 6546 VDFs						*Criteria DN: 8664 VDFs*					
n_p	0.10	42.1	9.88	8.87	3.98	13.6	0.62	76.2	18.7	16.9	7.94	25.8
n_α	0.02	2.25	0.24	0.15	0.10	0.29	0.03	4.75	0.64	0.53	0.23	0.88
n_i	0.18	66.3	9.24	8.47	4.49	12.2	0.43	98.8	20.2	16.3	8.92	27.8
n_{ec}	0.30	26.9	9.07	8.29	4.35	12.6	0.63	55.3	17.3	16.4	8.48	24.3
n_{eh}	0.002	4.45	0.42	0.27	0.17	0.49	0.002	6.87	0.58	0.43	0.26	0.70
n_{eb}	0.0009	2.29	0.23	0.16	0.10	0.28	0.001	3.50	0.24	0.18	0.10	0.30
n_{eff}	0.004	27.4	9.56	8.63	4.76	13.7	0.004	56.9	17.9	17.0	9.05	24.9
n_{eh}/n_{ec}	0.0006	0.30	0.05	0.04	0.02	0.07	0.0002	0.30	0.04	0.03	0.02	0.05
n_{eb}/n_{ec}	0.00004	0.30	0.03	0.03	0.01	0.04	0.00003	0.30	0.02	0.01	0.006	0.03
n_{eb}/n_{eh}	0.002	9.86	0.95	0.69	0.31	1.13	0.003	9.20	0.72	0.45	0.21	0.79

Table 9
(Continued)

n_s (cm^{-3})	$X_{\rm min}$[a]	$X_{\rm max}$	$\bar{X}$	$\tilde{X}$	$X_{25\%}$	$X_{75\%}$	$X_{\rm min}$	$X_{\rm max}$	$\bar{X}$	$\tilde{X}$	$X_{25\%}$	$X_{75\%}$
	Criteria LM: 12,988 VDFs							*Criteria HM: 2222 VDFs*				
n_p	0.10	76.2	14.5	11.4	6.06	20.6	0.80	45.3	17.1	13.2	7.31	26.5
n_α	0.02	4.75	0.44	0.25	0.12	0.65	0.06	2.16	0.56	0.42	0.22	0.84
n_i	0.18	98.8	15.0	11.1	6.93	19.2	2.78	50.5	18.5	15.3	7.84	29.0
$n_{\rm ec}$	0.30	55.3	13.4	11.2	6.49	18.5	2.50	39.0	16.0	14.3	7.99	23.5
$n_{\rm eh}$	0.002	6.87	0.48	0.33	0.19	0.59	0.004	6.55	0.73	0.55	0.35	0.91
$n_{\rm eb}$	0.0009	3.50	0.22	0.16	0.09	0.27	0.01	2.62	0.35	0.26	0.15	0.46
$n_{\rm eff}$	0.004	56.9	14.0	11.7	6.81	19.3	0.12	40.1	16.8	14.8	8.50	24.3
$n_{\rm eh}/n_{\rm ec}$	0.0002	0.30	0.05	0.03	0.02	0.06	0.001	0.23	0.05	0.04	0.02	0.07
$n_{\rm eb}/n_{\rm ec}$	0.00003	0.30	0.03	0.02	0.007	0.03	0.0005	0.21	0.03	0.02	0.01	0.05
$n_{\rm eb}/n_{\rm eh}$	0.002	9.86	0.82	0.50	0.24	0.98	0.01	9.18	0.78	0.50	0.28	0.87
	Criteria PE: 10,940 VDFs							*Criteria PA: 4270 VDFs*				
n_p	0.10	76.2	17.0	13.8	8.18	23.0	0.95	56.2	9.45	6.09	3.29	11.0
n_α	0.02	4.75	0.52	0.39	0.16	0.75	0.03	2.00	0.24	0.13	0.10	0.29
n_i	0.18	98.8	17.9	12.9	8.32	23.7	1.44	52.7	9.48	7.07	3.91	13.4
$n_{\rm ec}$	0.30	55.3	15.5	13.8	8.09	22.1	0.97	40.0	9.22	6.79	3.70	12.2
$n_{\rm eh}$	0.002	6.55	0.59	0.43	0.24	0.72	0.002	6.87	0.31	0.23	0.14	0.38
$n_{\rm eb}$	0.001	3.50	0.26	0.18	0.10	0.31	0.0009	3.33	0.19	0.14	0.09	0.26
$n_{\rm eff}$	0.004	56.9	16.2	14.4	8.47	22.8	0.05	40.2	9.60	7.22	3.96	12.5
$n_{\rm eh}/n_{\rm ec}$	0.0005	0.30	0.05	0.03	0.02	0.06	0.0002	0.30	0.05	0.03	0.02	0.06
$n_{\rm eb}/n_{\rm ec}$	0.00003	0.28	0.02	0.02	0.007	0.03	0.00004	0.30	0.03	0.03	0.01	0.04
$n_{\rm eb}/n_{\rm eh}$	0.002	9.86	0.77	0.49	0.21	0.89	0.005	9.65	0.94	0.65	0.35	1.13

Notes. For symbol definitions, see Appendix A.
[a] Header symbols match those of Table 2.

Table 10
Electron Beta Parameters

$\beta_{s,j}$ (N/A)	$X_{\rm min}$[a]	$X_{\rm max}$	$\bar{X}$	$\tilde{X}$	$X_{25\%}$	$X_{75\%}$	$X_{\rm min}$	$X_{\rm max}$	$\bar{X}$	$\tilde{X}$	$X_{25\%}$	$X_{75\%}$
	Criteria UP: 6546 VDFs							*Criteria DN: 8664 VDFs*				
$\beta_{\rm ec,\parallel}$	0.05	809	4.60	1.21	0.64	2.36	0.06	3313	2.89	0.91	0.51	1.70
$\beta_{\rm ec,\perp}$	0.05	811	4.45	1.20	0.58	2.34	0.04	3268	2.81	0.85	0.44	1.63
$\beta_{\rm ec,tot}$	0.05	811	4.50	1.21	0.59	2.34	0.05	3283	2.84	0.86	0.47	1.65
$\beta_{\rm eh,\parallel}$	0.0007	160	0.77	0.17	0.08	0.31	0.0001	375	0.27	0.08	0.03	0.14
$\beta_{\rm eh,\perp}$	0.002	162	0.78	0.17	0.08	0.32	0.0008	378	0.28	0.08	0.03	0.15
$\beta_{\rm eh,tot}$	0.001	161	0.78	0.17	0.08	0.32	0.0009	377	0.27	0.08	0.03	0.15
$\beta_{\rm eb,\parallel}$	0.0001	33.7	0.20	0.10	0.06	0.18	0.00002	33.2	0.07	0.03	0.01	0.06
$\beta_{\rm eb,\perp}$	0.0005	31.8	0.19	0.09	0.05	0.15	0.00003	46.4	0.07	0.03	0.01	0.06
$\beta_{\rm eb,tot}$	0.0005	32.4	0.20	0.09	0.05	0.16	0.00003	42.0	0.07	0.03	0.02	0.06
$\beta_{\rm eff,\parallel}$	0.004	977	5.44	1.43	0.81	2.66	0.0009	3721	3.20	1.01	0.57	1.84
$\beta_{\rm eff,\perp}$	0.002	983	5.30	1.41	0.74	2.63	0.0010	3693	3.11	0.94	0.51	1.77
$\beta_{\rm eff,tot}$	0.003	981	5.34	1.42	0.76	2.63	0.0009	3702	3.14	0.96	0.53	1.79
	Criteria LM: 12,988 VDFs							*Criteria HM: 2222 VDFs*				
$\beta_{\rm ec,\parallel}$	0.05	3313	2.30	0.93	0.56	1.83	0.19	1084	11.7	1.78	0.71	6.77
$\beta_{\rm ec,\perp}$	0.04	3268	2.23	0.87	0.49	1.81	0.09	1080	11.3	1.70	0.66	6.67
$\beta_{\rm ec,tot}$	0.05	3283	2.26	0.88	0.51	1.82	0.13	1081	11.5	1.72	0.69	6.67
$\beta_{\rm eh,\parallel}$	0.0001	375	0.28	0.09	0.04	0.18	0.0003	160	1.72	0.27	0.11	1.11
$\beta_{\rm eh,\perp}$	0.001	378	0.28	0.10	0.04	0.18	0.0008	162	1.74	0.28	0.11	1.08
$\beta_{\rm eh,tot}$	0.0010	377	0.28	0.10	0.04	0.18	0.0009	161	1.73	0.27	0.11	1.09
$\beta_{\rm eb,\parallel}$	0.00002	33.2	0.09	0.05	0.02	0.10	0.0002	33.7	0.39	0.13	0.03	0.35
$\beta_{\rm eb,\perp}$	0.00003	46.4	0.08	0.04	0.02	0.08	0.0007	31.8	0.40	0.11	0.03	0.38
$\beta_{\rm eb,tot}$	0.00003	42.0	0.08	0.05	0.02	0.09	0.0005	32.4	0.40	0.12	0.03	0.38
$\beta_{\rm eff,\parallel}$	0.0009	3721	2.62	1.06	0.66	2.10	0.007	1153	13.5	2.13	0.88	7.68
$\beta_{\rm eff,\perp}$	0.0010	3693	2.55	0.98	0.58	2.06	0.005	1153	13.2	2.03	0.79	7.77
$\beta_{\rm eff,tot}$	0.0009	3702	2.57	1.00	0.61	2.07	0.008	1153	13.3	2.06	0.82	7.74

Table 10
(Continued)

$\beta_{s,j}$ (N/A)	$X_{\min}$[a]	$X_{\max}$	$\bar{X}$	$\tilde{X}$	$X_{25\%}$	$X_{75\%}$	$X_{\min}$	$X_{\max}$	$\bar{X}$	$\tilde{X}$	$X_{25\%}$	$X_{75\%}$
	Criteria PE: 10,940 VDFs						*Criteria PA: 4270 VDFs*					
$\beta_{ec,\parallel}$	0.05	3313	4.49	1.05	0.57	2.43	0.11	15.8	1.36	0.85	0.59	1.52
$\beta_{ec,\perp}$	0.04	3268	4.37	0.99	0.50	2.43	0.06	15.2	1.27	0.65	0.48	1.41
$\beta_{ec,tot}$	0.05	3283	4.41	1.01	0.52	2.43	0.08	15.4	1.30	0.73	0.52	1.43
$\beta_{eh,\parallel}$	0.0001	375	0.61	0.12	0.05	0.25	0.0007	2.98	0.14	0.09	0.04	0.14
$\beta_{eh,\perp}$	0.0008	378	0.62	0.12	0.05	0.25	0.002	3.42	0.15	0.09	0.05	0.15
$\beta_{eh,tot}$	0.0009	377	0.62	0.12	0.05	0.25	0.002	3.27	0.14	0.09	0.04	0.15
$\beta_{eb,\parallel}$	0.00002	33.7	0.15	0.05	0.02	0.12	0.0001	1.60	0.08	0.05	0.03	0.09
$\beta_{eb,\perp}$	0.00003	46.4	0.14	0.05	0.02	0.11	0.002	1.92	0.07	0.04	0.02	0.07
$\beta_{eb,tot}$	0.00003	42.0	0.14	0.05	0.02	0.11	0.001	1.82	0.08	0.05	0.02	0.08
$\beta_{eff,\parallel}$	0.0009	3721	5.16	1.23	0.68	2.69	0.01	19.2	1.55	0.97	0.70	1.68
$\beta_{eff,\perp}$	0.0010	3693	5.05	1.16	0.62	2.67	0.01	19.5	1.46	0.79	0.58	1.64
$\beta_{eff,tot}$	0.0009	3702	5.08	1.18	0.64	2.68	0.01	19.4	1.49	0.86	0.62	1.66

Notes. For symbol definitions, see Appendix A.
[a] Header symbols match those of Table 2.

Table 11
Electron Temperature Ratio Parameters

Ratio	$X_{\min}$[a]	$X_{\max}$	$\bar{X}$	$\tilde{X}$	$X_{25\%}$	$X_{75\%}$	$X_{\min}$	$X_{\max}$	$\bar{X}$	$\tilde{X}$	$X_{25\%}$	$X_{75\%}$
	Criteria UP: 6546 VDFs						*Criteria DN: 8664 VDFs*					
$\mathcal{T}^{eh}_{ec\parallel}$	0.49	17.9	3.56	3.29	2.52	4.49	0.17	11.8	2.79	2.84	1.93	3.65
$\mathcal{T}^{eh}_{ec\perp}$	0.69	17.9	3.92	3.71	2.74	4.64	0.41	17.5	3.03	3.04	2.27	3.73
$\mathcal{T}^{eh}_{ec\,tot}$	0.64	16.3	3.79	3.54	2.69	4.59	0.34	12.8	2.93	2.97	2.16	3.68
$\mathcal{T}^{eb}_{ec\parallel}$	0.62	25.7	3.24	3.08	2.46	3.83	0.23	14.6	2.57	2.67	1.77	3.33
$\mathcal{T}^{eb}_{ec\perp}$	0.90	24.6	3.15	2.79	2.29	3.61	0.46	19.2	2.67	2.60	1.97	3.23
$\mathcal{T}^{eb}_{ec\,tot}$	0.86	25.0	3.18	2.87	2.45	3.59	0.42	14.3	2.63	2.61	1.97	3.22
$\mathcal{T}^{eb}_{eh\parallel}$	0.15	5.97	1.04	0.91	0.68	1.25	0.15	6.12	1.07	0.94	0.71	1.33
$\mathcal{T}^{eb}_{eh\perp}$	0.16	6.15	0.93	0.77	0.56	1.07	0.13	7.11	0.96	0.83	0.66	1.14
$\mathcal{T}^{eb}_{eh\,tot}$	0.20	6.08	0.96	0.81	0.62	1.12	0.17	4.91	0.98	0.88	0.69	1.15
$\mathcal{T}^{eh}_{eff\parallel}$	0.50	17.4	3.07	2.87	2.20	3.88	0.17	10.6	2.60	2.64	1.80	3.39
$\mathcal{T}^{eh}_{eff\perp}$	0.72	16.8	3.33	3.21	2.40	4.03	0.43	15.8	2.81	2.80	2.11	3.46
$\mathcal{T}^{eh}_{eff\,tot}$	0.65	15.2	3.24	3.07	2.33	3.98	0.37	11.8	2.73	2.75	2.02	3.43
$\mathcal{T}^{eb}_{eff\parallel}$	0.36	19.6	2.78	2.68	2.16	3.26	0.24	14.2	2.40	2.49	1.65	3.09
$\mathcal{T}^{eb}_{eff\perp}$	0.66	18.7	2.70	2.39	2.00	3.03	0.46	18.5	2.48	2.36	1.83	3.02
$\mathcal{T}^{eb}_{eff\,tot}$	0.71	19.0	2.73	2.46	2.14	3.05	0.43	13.4	2.44	2.41	1.84	3.02
	Criteria LM: 12,988 VDFs						*Criteria HM: 2222 VDFs*					
$\mathcal{T}^{eh}_{ec\parallel}$	0.28	17.9	3.10	2.97	2.17	4.00	0.17	9.76	3.22	3.20	2.53	3.72
$\mathcal{T}^{eh}_{ec\perp}$	0.57	17.9	3.38	3.25	2.37	4.11	0.41	11.2	3.52	3.34	2.84	3.94
$\mathcal{T}^{eh}_{ec\,tot}$	0.50	16.3	3.27	3.17	2.32	4.07	0.34	9.89	3.41	3.29	2.77	3.86
$\mathcal{T}^{eb}_{ec\parallel}$	0.26	16.6	2.94	2.92	2.22	3.59	0.23	25.7	2.35	2.25	1.53	2.98
$\mathcal{T}^{eb}_{ec\perp}$	0.48	19.2	2.93	2.73	2.18	3.42	0.46	24.6	2.58	2.37	1.80	3.17
$\mathcal{T}^{eb}_{ec\,tot}$	0.47	15.1	2.92	2.79	2.33	3.39	0.42	25.0	2.49	2.26	1.79	3.10
$\mathcal{T}^{eb}_{eh\parallel}$	0.15	6.12	1.09	0.97	0.72	1.36	0.20	5.82	0.83	0.75	0.55	0.95
$\mathcal{T}^{eb}_{eh\perp}$	0.13	7.11	0.97	0.83	0.63	1.16	0.16	5.33	0.78	0.74	0.57	0.91
$\mathcal{T}^{eb}_{eh\,tot}$	0.17	6.08	1.00	0.88	0.67	1.18	0.20	5.49	0.79	0.73	0.59	0.91
$\mathcal{T}^{eh}_{eff\parallel}$	0.29	17.4	2.79	2.70	2.00	3.61	0.17	8.78	2.84	2.83	2.26	3.36
$\mathcal{T}^{eh}_{eff\perp}$	0.56	16.8	3.03	2.94	2.17	3.73	0.43	10.6	3.07	2.96	2.55	3.49
$\mathcal{T}^{eh}_{eff\,tot}$	0.56	15.2	2.94	2.88	2.12	3.67	0.37	8.89	2.98	2.89	2.46	3.44
$\mathcal{T}^{eb}_{eff\parallel}$	0.29	14.8	2.64	2.65	2.01	3.22	0.24	19.6	2.05	1.97	1.38	2.61
$\mathcal{T}^{eb}_{eff\perp}$	0.48	18.7	2.63	2.41	1.97	3.08	0.46	18.7	2.21	2.12	1.63	2.73
$\mathcal{T}^{eb}_{eff\,tot}$	0.48	13.7	2.63	2.48	2.08	3.09	0.43	19.0	2.15	2.01	1.61	2.66

Table 11
(Continued)

Ratio	$X_{\min}$[a]	$X_{\max}$	$\bar{X}$	$\tilde{X}$	$X_{25\%}$	$X_{75\%}$	$X_{\min}$	$X_{\max}$	$\bar{X}$	$\tilde{X}$	$X_{25\%}$	$X_{75\%}$
	Criteria PE: 10,940 VDFs						*Criteria PA: 4270 VDFs*					
$\mathcal{T}_{ec\parallel}^{eh}$	0.17	14.4	3.17	3.03	2.29	3.96	0.28	17.9	2.97	2.97	1.92	4.00
$\mathcal{T}_{ec\perp}^{eh}$	0.41	15.8	3.41	3.23	2.47	4.05	0.70	17.9	3.39	3.39	2.40	4.22
$\mathcal{T}_{ec\,tot}^{eh}$	0.34	12.7	3.32	3.17	2.44	4.01	0.50	16.3	3.21	3.28	2.27	4.14
$\mathcal{T}_{ec\parallel}^{eb}$	0.23	25.7	2.89	2.88	2.09	3.56	0.46	14.6	2.76	2.76	2.10	3.46
$\mathcal{T}_{ec\perp}^{eb}$	0.46	24.6	2.97	2.74	2.19	3.46	0.52	19.2	2.64	2.56	1.92	3.20
$\mathcal{T}_{ec\,tot}^{eb}$	0.42	25.0	2.94	2.81	2.25	3.42	0.53	13.5	2.67	2.60	2.16	3.21
$\mathcal{T}_{eh\parallel}^{eb}$	0.15	5.97	1.04	0.92	0.67	1.29	0.17	6.12	1.09	0.94	0.75	1.33
$\mathcal{T}_{eh\perp}^{eb}$	0.13	7.11	0.98	0.83	0.62	1.18	0.16	4.84	0.85	0.77	0.60	0.98
$\mathcal{T}_{eh\,tot}^{eb}$	0.17	6.08	0.99	0.85	0.66	1.19	0.25	4.58	0.92	0.84	0.66	1.05
$\mathcal{T}_{eff\parallel}^{eh}$	0.17	13.0	2.83	2.74	2.11	3.55	0.29	17.4	2.71	2.69	1.73	3.62
$\mathcal{T}_{eff\perp}^{eh}$	0.43	14.4	3.02	2.92	2.29	3.65	0.73	16.8	3.07	3.05	2.14	3.78
$\mathcal{T}_{eff\,tot}^{eh}$	0.37	11.1	2.95	2.86	2.24	3.60	0.56	15.2	2.93	2.96	2.03	3.73
$\mathcal{T}_{eff\parallel}^{eb}$	0.24	19.6	2.58	2.61	1.90	3.20	0.47	14.2	2.51	2.49	1.87	3.10
$\mathcal{T}_{eff\perp}^{eb}$	0.46	18.7	2.65	2.43	1.98	3.08	0.53	18.7	2.38	2.24	1.74	2.84
$\mathcal{T}_{eff\,tot}^{eb}$	0.43	19.0	2.62	2.49	2.02	3.08	0.58	13.1	2.42	2.30	1.94	2.87

Notes. For symbol definitions, see Appendix A.
[a] Header symbols match those of Table 2.

Table 12
Electron Temperature Anisotropy Parameters

Anisotropy	$X_{\min}$[a]	$X_{\max}$	$\bar{X}$	$\tilde{X}$	$X_{25\%}$	$X_{75\%}$	$X_{\min}$	$X_{\max}$	$\bar{X}$	$\tilde{X}$	$X_{25\%}$	$X_{75\%}$
	Criteria UP: 6546 VDFs						*Criteria DN: 8664 VDFs*					
$\mathcal{A}_{ec}$	0.50	1.15	0.94	0.98	0.91	1.00	0.38	1.56	0.92	0.98	0.90	1.01
$\mathcal{A}_{eh}$	0.31	10.9	1.05	1.03	0.95	1.12	0.24	15.0	1.07	1.04	0.96	1.12
$\mathcal{A}_{eb}$	0.25	15.2	0.95	0.90	0.75	1.07	0.13	14.1	1.04	0.96	0.82	1.13
$\mathcal{A}_{eff}$	0.45	2.52	0.95	0.97	0.92	1.00	0.35	2.80	0.93	0.98	0.91	1.01
	Criteria LM: 12,988 VDFs						*Criteria HM: 2222 VDFs*					
$\mathcal{A}_{ec}$	0.38	1.56	0.93	0.98	0.91	1.01	0.42	1.21	0.91	0.96	0.85	0.99
$\mathcal{A}_{eh}$	0.28	15.0	1.06	1.04	0.95	1.13	0.24	7.03	1.06	1.03	0.98	1.08
$\mathcal{A}_{eb}$	0.13	15.2	0.99	0.92	0.77	1.09	0.33	3.65	1.08	1.02	0.85	1.19
$\mathcal{A}_{eff}$	0.35	2.80	0.94	0.98	0.92	1.01	0.40	1.96	0.92	0.97	0.87	1.00
	Criteria PE: 10,940 VDFs						*Criteria PA: 4270 VDFs*					
$\mathcal{A}_{ec}$	0.38	1.51	0.94	0.98	0.93	1.01	0.44	1.56	0.89	0.96	0.80	1.01
$\mathcal{A}_{eh}$	0.24	15.0	1.05	1.03	0.95	1.11	0.31	5.44	1.09	1.04	0.96	1.15
$\mathcal{A}_{eb}$	0.13	14.1	1.04	0.96	0.81	1.15	0.18	15.2	0.89	0.88	0.69	1.01
$\mathcal{A}_{eff}$	0.35	2.80	0.95	0.98	0.94	1.01	0.45	1.50	0.90	0.95	0.83	1.01

Notes. For symbol definitions, see Appendix A.
[a] Header symbols match those of Table 2.

Table 13
Coulomb Collision Rates [# per Week]

$\nu_{ss'}$	$X_{\min}$[a]	$X_{\max}$	$\bar{X}$	$\tilde{X}$	$X_{25\%}$	$X_{75\%}$	$X_{\min}$	$X_{\max}$	$\bar{X}$	$\tilde{X}$	$X_{25\%}$	$X_{75\%}$
	Criteria UP: 6546 VDFs						*Criteria DN: 8664 VDFs*					
ν_{ecc}	0.05	16.4	4.68	3.90	2.00	6.68	0.05	22.3	6.01	5.93	2.66	8.99
ν_{ehh}	0.00007	1.91	0.05	0.02	0.01	0.05	0.00006	3.14	0.06	0.03	0.02	0.06
ν_{ebb}	0.00007	0.58	0.03	0.02	0.008	0.04	0.00007	1.42	0.03	0.02	0.008	0.03
ν_{ehc}	0.02	40.9	1.95	1.40	0.66	2.33	0.03	49.3	2.68	2.09	0.94	3.07
ν_{ebc}	0.03	44.3	3.77	1.66	0.87	3.50	0.02	57.8	5.36	2.58	1.34	4.27
ν_{ehb}	0.00009	4.54	0.07	0.03	0.02	0.06	0.00008	8.76	0.07	0.04	0.02	0.08
ν_{ecp}	0.009	9.60	2.57	2.17	1.15	3.53	0.03	14.7	3.30	3.18	1.20	4.86

Table 13
(Continued)

$\nu_{ss'}$	$X_{\min}$[a]	$X_{\max}$	$\bar{X}$	$\tilde{X}$	$X_{25\%}$	$X_{75\%}$	$X_{\min}$	$X_{\max}$	$\bar{X}$	$\tilde{X}$	$X_{25\%}$	$X_{75\%}$
ν_{ehp}	0.004	5.86	0.47	0.35	0.17	0.65	0.008	16.1	0.76	0.60	0.29	0.93
ν_{ebp}	0.004	4.88	0.55	0.40	0.20	0.68	0.01	8.78	0.82	0.65	0.37	1.01
$\nu_{ec\alpha}$	0.02	2.59	0.24	0.15	0.09	0.26	0.009	3.11	0.43	0.30	0.17	0.60
$\nu_{eh\alpha}$	0.0008	0.61	0.05	0.02	0.01	0.06	0.002	1.53	0.11	0.07	0.03	0.14
$\nu_{eb\alpha}$	0.003	0.41	0.05	0.03	0.02	0.07	0.004	1.55	0.12	0.09	0.04	0.16
ν_{pp}	0.001	3.97	0.65	0.36	0.12	0.91	0.0001	2.29	0.43	0.28	0.09	0.58
$\nu_{\alpha\alpha}$	0.002	1.60	0.16	0.08	0.03	0.21	0.004	0.34	0.05	0.03	0.02	0.05
$\nu_{p\alpha}$	0.0003	0.52	0.03	0.02	0.007	0.03	0.0003	0.10	0.02	0.01	0.008	0.02
	Criteria LM: 12,988 VDFs						*Criteria HM: 2222 VDFs*					
ν_{ecc}	0.05	22.3	5.62	4.76	2.51	8.21	0.45	10.4	4.35	5.13	1.20	6.43
ν_{ehh}	0.00006	3.14	0.06	0.03	0.01	0.06	0.0002	1.44	0.04	0.03	0.02	0.06
ν_{ebb}	0.00007	1.42	0.03	0.02	0.008	0.03	0.0005	0.80	0.04	0.02	0.01	0.05
ν_{ehc}	0.02	49.3	2.51	1.82	0.82	2.95	0.07	9.34	1.51	1.54	0.64	2.12
ν_{ebc}	0.02	57.8	4.73	2.16	1.12	3.83	0.16	29.1	4.38	2.29	0.86	4.18
ν_{ehb}	0.00008	8.76	0.07	0.03	0.02	0.07	0.00010	2.09	0.07	0.04	0.02	0.09
ν_{ecp}	0.009	14.7	3.07	2.60	1.25	4.50	0.12	7.48	2.48	2.99	0.52	3.82
ν_{ehp}	0.004	16.1	0.66	0.49	0.24	0.83	0.009	3.32	0.47	0.48	0.19	0.66
ν_{ebp}	0.004	8.78	0.69	0.51	0.30	0.86	0.04	7.13	0.78	0.59	0.24	1.12
$\nu_{ec\alpha}$	0.009	3.11	0.35	0.23	0.12	0.50	0.05	0.99	0.30	0.25	0.15	0.43
$\nu_{eh\alpha}$	0.0008	1.53	0.08	0.04	0.02	0.10	0.006	0.80	0.06	0.04	0.02	0.08
$\nu_{eb\alpha}$	0.003	0.92	0.08	0.05	0.02	0.12	0.003	1.55	0.12	0.07	0.04	0.14
ν_{pp}	0.0001	3.97	0.51	0.28	0.11	0.68	0.005	3.09	0.69	0.61	0.06	0.94
$\nu_{\alpha\alpha}$	0.002	1.60	0.12	0.06	0.02	0.11	0.005	0.44	0.14	0.11	0.05	0.24
$\nu_{p\alpha}$	0.0003	0.52	0.02	0.01	0.008	0.02	0.001	0.15	0.03	0.02	0.006	0.05
	Criteria PE: 10,940 VDFs						*Criteria PA: 4270 VDFs*					
ν_{ecc}	0.05	21.6	5.96	5.85	3.04	8.51	0.26	22.3	4.12	3.46	1.00	5.59
ν_{ehh}	0.00006	1.91	0.06	0.03	0.02	0.07	0.00008	3.14	0.04	0.02	0.01	0.04
ν_{ebb}	0.00007	1.03	0.03	0.02	0.008	0.03	0.0001	1.42	0.02	0.02	0.008	0.03
ν_{ehc}	0.02	49.3	2.62	1.99	0.95	2.98	0.05	40.9	1.74	1.13	0.59	2.24
ν_{ebc}	0.02	57.8	5.01	2.49	1.32	4.31	0.09	46.4	3.84	1.52	0.75	3.27
ν_{ehb}	0.00008	4.54	0.08	0.04	0.02	0.08	0.00009	8.76	0.06	0.02	0.01	0.05
ν_{ecp}	0.009	12.1	3.31	3.21	1.72	4.60	0.11	14.7	2.15	1.49	0.56	2.78
ν_{ehp}	0.004	16.1	0.71	0.57	0.28	0.89	0.01	6.65	0.42	0.30	0.16	0.57
ν_{ebp}	0.004	8.78	0.79	0.61	0.36	0.98	0.02	6.56	0.47	0.35	0.20	0.61
$\nu_{ec\alpha}$	0.009	3.11	0.40	0.26	0.14	0.56	0.02	1.26	0.20	0.14	0.10	0.24
$\nu_{eh\alpha}$	0.0008	1.53	0.09	0.06	0.03	0.12	0.001	1.37	0.05	0.03	0.02	0.05
$\nu_{eb\alpha}$	0.003	1.55	0.10	0.07	0.03	0.14	0.004	0.58	0.05	0.03	0.02	0.06
ν_{pp}	0.0001	3.97	0.61	0.37	0.16	0.80	0.001	1.98	0.33	0.15	0.02	0.45
$\nu_{\alpha\ \alpha}$	0.002	1.60	0.13	0.06	0.02	0.15	0.005	0.23	0.06	0.06	0.02	0.08
$\nu_{p\alpha}$	0.0003	0.52	0.02	0.02	0.009	0.03	0.0003	0.08	0.01	0.01	0.003	0.02

Notes. For symbol definitions, see Appendix A.
[a] Header symbols match those of Table 2.

Appendix D
Previous Electron Studies

In this appendix, we summarize in Tables 14–18 the observations of previous electron velocity moments near 1 au, similar to the appendices in Wilson et al. (2018). The symbols/parameters are the same as elsewhere herein. The results from the present three-part study will be denoted as "this work" in the following tables. Note that the subscript for the total electron distribution parameters in previous work was simply e in most cases, and it was not always clear whether the results were the equivalent of the eff or int subscripts in the current three-part study or something else (e.g., numerical velocity moments). Thus, we denote these parameters with only a subscript e when ambiguous or different from the methods used to calculate the effective and integrated results associated with eff and int, respectively.

Prior to presenting the tables of previous results, it is worth noting that differences in analysis and fit parameter calculation/determination exist between this three-part study and some previous work. For instance, the electron velocity moments presented in Wilson et al. (2007, 2009, 2010, 2013a, 2013b, 2014a, 2014b) are all computed using a numerical summation over energy-angle bins with instrument-specific corrections and differential volumes. There are known limitations/issues with such an approach (e.g., Song et al. 1997; Paschmann & Daly 1998; Gershman et al. 2015), but it is the most common method for calculating the velocity moments of any species. Note that for these studies the velocity moment results for the entire distribution are denoted with a subscript e instead of eff or int, as the methods for calculating the parameters are different.

Table 14
Measurements of Electron Temperatures (eV) at 1 au

References	Parameter	Spacecraft	Notes	X_{min}–X_{max}	$\bar{X}$[a]
Skoug et al. (2000)	$T_{ec,tot}$	*ACE*	SW[b]	∼3–60	
	$T_{eh,tot}$			∼26–560	
Masters et al. (2011)	$\Delta T_{e,tot}$	*Cassini*	KBS[c]	∼10–120	
Lefebvre et al. (2007)	$\langle T_{e,tot}\rangle_{up}$	*Cluster*	BS[d]	∼14.3–22.8	
	$\langle T_{e,tot}\rangle_{dn}$			∼25.8–90.8	
Schwartz et al. (2011)	$\langle T_{e,\parallel}\rangle_{up}$			∼17.2–51.7	
	$\langle T_{e,\perp}\rangle_{up}$			∼12.9–34.5	
	$\langle T_{e,\parallel}\rangle_{dn}$			∼73.2–103.4	
	$\langle T_{e,\perp}\rangle_{dn}$			∼73.2–103.4	
Viñas et al. (2010)	$T_{eb,tot}$		SW	∼20–50	
Hull et al. (1998)	$\langle T_{e,tot}\rangle_{up}$	*Galileo*	BS		∼12.9
	$\langle T_{ec,\parallel}\rangle_{up}$				∼16.4
	$\langle T_{ec,\perp}\rangle_{up}$				∼11.2
	$\langle T_{e,tot}\rangle_{dn}$				∼14.6
	$\langle T_{ec,\parallel}\rangle_{dn}$				∼16.4
	$\langle T_{ec,\perp}\rangle_{dn}$				∼13.8
Pilipp et al. (1990)	$T_{ec,tot}$	*Helios 1* and *2*	Slow SW[e]	∼7–13	
	$T_{ec,tot}$		Fast SW	∼6–9	
Feldman et al. (1973)	$\langle T_{e,tot}\rangle_{up}$	*Imp 6*	BS	∼4.3–24.0	
	$\langle T_{ec,tot}\rangle_{up}$			∼2.6–22.4	
Feldman et al. (1975)	$T_{ec,tot}$	*Imp 7* and *8*	SW		∼10.7–10.9
	$T_{eh,tot}$				∼58–60
Feldman et al. (1978)	$T_{ec,tot}$	*Imp 6*, *7*, and *8*	Fast SW		∼56
	$T_{eh,tot}$				∼7.3
Feldman et al. (1979)	$T_{ec,tot}$		SW	∼7.8–16	
	$T_{eh,\parallel}$			∼49–83	
Feldman et al. (1983a)	$\langle T_{ec,tot}\rangle_{dn}$	*ISEE 2*	BS	∼23–139	
Feldman et al. (1983b)	$\langle T_{e,tot}\rangle_{up}$	*ISEE 3*	IPS[f]	∼8.6–19.8	
Hull et al. (2000)	$\langle T_{e,tot}\rangle_{up}$	*ISEE 1*	BS	∼6.0–31.9	∼14.6
	$\Delta T_{e,tot}$			<10 to >200	∼30
Hull & Scudder (2000)	$\Delta T_{e,tot}$			∼7–205	
	$\Delta T_{e,\parallel}$			∼6–205	
	$\Delta T_{e,\perp}$			∼8–200	
Schwartz et al. (1988)	$\Delta T_{e,tot}$	*ISEE 3*	BS and IPS	∼8.6–198	
Thomsen et al. (1985)	$\Delta T_{e,\parallel}$	*ISEE 1* and *2*	BS	∼14–41	
	$\Delta T_{e,\perp}$			∼13–52	
Thomsen et al. (1987)	$\Delta T_{e,tot}$			∼9.5–198	
	$\langle T_{e,tot}\rangle_{up}$			∼5.2–31.9	
	$\langle T_{e,tot}\rangle_{dn}$			∼28–224	
Thomsen et al. (1993)	$\Delta T_{e,tot}$	*ISEE 2*		∼7.8–172	
Chen et al. (2018)	$T_{e,\parallel}$	*MMS*	BS	∼25–210	
	$T_{e,\perp}$			∼25–150	
Wilson et al. (2014a) and	$\langle T_{e,tot}\rangle_{up}$	*THEMIS*	BS	∼7.9–31.2	
Wilson et al. (2014b)	$\langle T_{e,tot}\rangle_{dn}$			∼30.5–81.5	
Maksimovic et al. (1997)	$T_{ec,tot}$	*Ulysses*	SW	∼4.6–15.5	
	$T_{eh,tot}$	*Ulysses*		∼49–86	
Hull et al. (2001)	$\langle T_{e,tot}\rangle_{up}$	*Wind*	BS		∼12.1
	$\langle T_{e,tot}\rangle_{dn}$				∼29.3
Maksimovic et al. (2005)	$T_{ec,tot}$		SW	∼6.5–10	
	$T_{eh,tot}$			∼14–43	
Tao et al. (2016a)	$T_{eh,tot}$			∼21–62	
	$T_{eb,tot}$			∼23–68	
Ogilvie et al. (2000)	$T_{eb,tot}$			∼100–150	
Fitzenreiter et al. (2003)	$\Delta T_{e,tot}$		IPS	∼4.3–41.6	
Pulupa et al. (2010)	$\langle T_{e,tot}\rangle_{up}$			∼4.1–36.8	

Table 14
(Continued)

References	Parameter	Spacecraft	Notes	$X_{\min}$–$X_{\max}$	$\bar{X}$[a]
	$\langle T_{e,\mathrm{tot}} \rangle_{\mathrm{dn}}$			∼7.3–60.2	
Wilson et al. (2009)	$T_{e,\mathrm{tot}}$			∼11–76	
	$T_{e,\parallel}$			∼10–80	
	$T_{e,\perp}$			∼11–75	
	$T_{\mathrm{ec,tot}}$			∼9–38	
	$T_{\mathrm{ec},\parallel}$			∼9–37	
	$T_{\mathrm{ec},\perp}$			∼10–38	
	$T_{\mathrm{eh,tot}}$			∼43–175	
	$T_{\mathrm{eh},\parallel}$			∼39–190	
	$T_{\mathrm{eh},\perp}$			∼44–189	
Wilson et al. (2010)	$T_{e,\mathrm{tot}}$			∼10–64	
	$T_{e,\parallel}$			∼9.8–90	
	$T_{e,\perp}$			∼9.7–90	
	$T_{\mathrm{ec,tot}}$			∼6–37	
	$T_{\mathrm{ec},\parallel}$			∼6–55	
	$T_{\mathrm{ec},\perp}$			∼6–38	
	$T_{\mathrm{eh,tot}}$			∼35–220	
	$T_{\mathrm{eh},\parallel}$			∼35–250	
	$T_{\mathrm{eh},\perp}$			∼35–240	
Wilson et al. (2012)	$T_{e,\mathrm{tot}}$			∼18.9–60.6	∼41.6
	$T_{\mathrm{ec,tot}}$			∼16.6–38.7	∼31.1
	$T_{\mathrm{ec},\parallel}$			∼16.5–42.2	∼30.2
	$T_{\mathrm{eh},\parallel}$			∼117–290	∼208
	$T_{\mathrm{eh},\perp}$			∼113–294	∼201
Wilson et al. (2013b)	$T_{e,\mathrm{tot}}$			∼26–64	
	$T_{e,\parallel}$			∼24–64	
	$T_{e,\perp}$			∼25–65	
	$T_{\mathrm{ec,tot}}$			∼24–54	
	$T_{\mathrm{ec},\parallel}$			∼23–57	
	$T_{\mathrm{ec},\perp}$			∼23–55	
	$T_{\mathrm{eh,tot}}$			∼160–300	
	$T_{\mathrm{eh},\parallel}$			∼115–280	
	$T_{\mathrm{eh},\perp}$			∼160–315	
This work	$T_{\mathrm{ec},\parallel}$	*Wind*	IPS/AT[g]	∼6–89	∼19.1
	$T_{\mathrm{ec},\perp}$			∼5–63	∼16.4
	$T_{\mathrm{ec,tot}}$			∼5–67	∼17.3
	$T_{\mathrm{eh},\parallel}$			∼12–249	∼49.0
	$T_{\mathrm{eh},\perp}$			∼11–255	∼50.7
	$T_{\mathrm{eh,tot}}$			∼12–222	∼50.2
	$T_{\mathrm{eb},\parallel}$			∼12–280	∼44.2
	$T_{\mathrm{eb},\perp}$			∼12–277	∼42.6
	$T_{\mathrm{eb,tot}}$			∼12–269	∼43.1
	$T_{\mathrm{eff},\parallel}$			∼7–167	∼20.6
	$T_{\mathrm{eff},\perp}$			∼5–170	∼18.1
	$T_{\mathrm{eff,tot}}$			∼6–169	∼18.9
	$T_{\mathrm{int},\parallel}$			∼9–80	∼20.6
	$T_{\mathrm{int},\perp}$			∼8–70	∼17.2
	$T_{\mathrm{int,tot}}$			∼8–69	∼18.3

Notes. OMNI is a data set composed of multiple spacecraft from SPDF/CDAWeb, where All refers to 1963–present and Late to 1978–present. For symbol definitions, see Appendix A.
[a] Mean or average.
[b] SW ≡ Solar wind, a generic term for ambient/all solar wind conditions.
[c] Kronian bow shock.
[d] Terrestrial bow shock.
[e] Fast and Slow SW are typically defined as bulk flow speed above or below, respectively, some threshold (typically ∼350–500 km s^{-1}).
[f] Interplanetary shock.
[g] AT ≡ selection *Criteria AT* defined in Section 2.

Table 15
Measurements of Electron Densities (cm^{-3}) at 1 au

References	Parameter	Spacecraft	Notes	X_{min}–X_{max}	$\bar{X}$
Skoug et al. (2000)	n_{ec}	*ACE*	SW and ICME		∼7.6–10.2
	n_{eh}				∼0.11–0.19
	n_{eh}/n_{ec}				∼0.027–0.028
Lefebvre et al. (2007)	$\langle n_e \rangle_{up}$	*Cluster*	BS		∼6.6–11.0
	$\langle n_e \rangle_{dn}$				∼19.3–37.8
Viñas et al. (2010)	n_e		SW	∼14–19	
	n_{eb}			∼0.05–0.20	
	n_{eb}/n_e			∼0.0025–0.02	
Hull et al. (1998)	$\langle n_e \rangle_{up}$	*Galileo*	BS		∼6.7
	$\langle n_e \rangle_{dn}$				∼8.5
Štverák et al. (2009)	n_{ec}	*Helios 1* and	Slow SW	∼7–10	
	n_{eh}	*Cluster*		∼0.20–0.33	
	n_{eb}			∼0.18–0.28	
	n_{eh}/n_e			∼0.038–0.045	
	n_{eb}/n_e			∼0.029–0.039	
	n_{ec}		Fast SW	∼4–6	
	n_{eh}			∼0.20–0.36	
	n_{eb}			∼0.17–0.29	
	n_{eh}/n_e			∼0.041–0.071	
	n_{eb}/n_e			∼0.025–0.051	
Feldman et al. (1975)	n_e	*Imp 7*	SW		∼9.0–11.3
	n_{eh}	and *Imp 8*			∼0.31–0.56
	n_{eh}/n_e				∼0.033–0.071
Feldman et al. (1979)	n_{eh}/n_e	*Imp 6*, *7*, and *8*		∼0.015–0.075	
Feldman et al. (1983b)	$\langle n_e \rangle_{up}$	*ISEE 3*	IPS	∼2.0–19.1	
	$\langle n_e \rangle_{dn}$			∼10.0–23.0	
	$\mathcal{R}_{ne}$			∼1.2–4.2	
Hull et al. (2000)	$\langle n_e \rangle_{up}$	*ISEE 1*	BS	<1 to >55	∼10
Phillips et al. (1989b)	n_e	*ISEE 3*	SW	<1 to >30	
	n_{ec}			∼1–30	
Maksimovic et al. (1997)	n_{ec}	*Ulysses*		∼0.49–4.81	
	n_{eh}			∼0.06–0.18	
Hull et al. (2001)	$\langle n_e \rangle_{up}$	*Wind*	BS		∼17
	$\langle n_e \rangle_{dn}$				∼48
Maksimovic et al. (2005)	n_e		SW	∼2.7–4.0	
	n_{eh}			∼0.23–0.38	
	n_{ec}/n_e			∼0.80–0.99	
	n_{eh}/n_e			∼0.075–0.11	
	n_{eb}/n_e			∼0.0015–0.02	
Nieves-Chinchilla & Viñas (2008)	n_e		ICME	∼0.5–40	
Pulupa et al. (2010)	$\langle n_e \rangle_{up}$		IPS	∼1–24	
	$\langle n_e \rangle_{dn}$			∼3–50	
Salem et al. (2001)	n_e		SW	∼2–90	
Tao et al. (2016b)	n_{eh}			∼0.018–0.29	
	n_{eb}			∼0.0017–0.08	
	n_{eb}/n_{eh}			∼0.025–0.88	
Wilson et al. (2009)	n_{ec}		IPS	∼4.7–10.4	
	n_{eh}			∼0.023–0.051	
Wilson et al. (2010)	n_{ec}			∼3–25	
	n_{eh}			∼0.03–1.10	
This work	n_{ec}	*Wind*	IPS/AT	∼0.3–55	∼13.8
	n_{eh}			∼0.002–7	∼0.51
	n_{eb}			∼0.001–4	∼0.24
	n_{eff}			∼0.004–57	∼14.4
	n_{int}			∼0.39–57	∼14.6
	n_{eh}/n_{ec}			∼0.0002–0.3	∼0.05
	n_{eb}/n_{ec}			∼0.00003–0.3	∼0.03
	n_{eb}/n_{eh}			∼0.002–10	∼0.82

Note. Definitions/symbols are the same as in Table 14. For symbol definitions, see Appendix A.

Table 16
Measurements of Electron Temperature Ratios at 1 au

References	Parameter	Spacecraft	Notes	X_{min}–X_{max}	$\bar{X}$
Skoug et al. (2000)	$\mathcal{T}^{eh}_{ec\,tot}$	*ACE*	SW	∼2–40	∼7.25
Feldman et al. (1975)	$\mathcal{T}^{eh}_{ec\,tot}$	*Imp 7* and *8*	SW		∼5.5–7.2
Bame et al. (1979)	$\mathcal{R}_{Te,tot}$	*ISEE 1* and *2*	BS	∼1.3–9.5	∼2.7
Thomsen et al. (1985)	$\mathcal{R}_{Te,\perp}$			∼1.7–3.5	
Thomsen et al. (1987)	$\mathcal{R}_{Te,tot}$			∼1.0–19.6	
Feldman et al. (1983b)	$\mathcal{R}_{Te,tot}$	*ISEE 3*	IPS	∼1.0–3.0	
Pulupa et al. (2010)	$\mathcal{R}_{Te,tot}$	*Wind*	IPS	∼1.0–4.0	
Wilson et al. (2009)	$\mathcal{T}^{eh}_{ec\parallel}$			∼3.5–12.8	
	$\mathcal{T}^{eh}_{ec\perp}$			∼4.4–10.9	
Wilson et al. (2012)	$\mathcal{T}^{eh}_{ec\parallel}$			∼3.82–8.38	∼6.78
	$\mathcal{T}^{eh}_{ec\perp}$			∼5.53–7.10	∼6.61
This work	$\mathcal{T}^{eh}_{ec\parallel}$	*Wind*	IPS/AT	∼0.2–18	∼3.11
	$\mathcal{T}^{eh}_{ec\perp}$			∼0.4–18	∼3.40
	$\mathcal{T}^{eh}_{ec\,tot}$			∼0.3–16	∼3.29
	$\mathcal{T}^{eb}_{ec\parallel}$			∼0.2–26	∼2.86
	$\mathcal{T}^{eb}_{ec\perp}$			∼0.5–25	∼2.88
	$\mathcal{T}^{eb}_{ec\,tot}$			∼0.4–25	∼2.86
	$\mathcal{T}^{eb}_{eh\parallel}$			∼0.2–6	∼1.06
	$\mathcal{T}^{eb}_{eh\perp}$			∼0.1–7	∼0.95
	$\mathcal{T}^{eb}_{eh\,tot}$			∼0.2–6	∼0.97

Note. Definitions/symbols are the same as in Tables 14. For symbol definitions, see Appendix A.

Table 17
Measurements of Electron Betas at 1 au

Reference	Parameter	Spacecraft	Notes	X_{min}–X_{max}	$\bar{X}$
Lacombe et al. (2014)	$\beta_{e,tot}$	*Cluster*	SW	∼0.09–25	
Lacombe et al. (2017)	$\beta_{e,\parallel}$			∼0.08–3.9	
Lefebvre et al. (2007)	$\langle\beta_{e,tot}\rangle_{up}$				∼0.45–5.99
	$\langle\beta_{e,tot}\rangle_{dn}$				∼0.63–3.40
Viñas et al. (2010)	$\beta_{e,\parallel}$			∼0.4–1.0	
	$\beta_{eb,\parallel}$			∼1.0–4.0	
Hull et al. (1998)	$\langle\beta_{e,tot}\rangle_{up}$	*Galileo*	BS		∼0.46
	$\langle\beta_{e,tot}\rangle_{dn}$				∼0.41
Štverák et al. (2008)	$\beta_{ec,\parallel}$	*Helios 1* and	Slow SW	∼0.04–40	
	$\beta_{eh,\parallel}$	*Cluster*		∼0.002–15	
	$\beta_{ec,\parallel}$		Fast SW	∼0.025–1.2	
	$\beta_{eh,\parallel}$			∼0.002–4.0	
Lazar et al. (2017)	$\beta_{eh,\parallel}$	HCU[a]	SW	∼0.001–80	
Hull et al. (2000)	$\langle\beta_{e,tot}\rangle_{up}$	*ISEE 1*	BS	∼0.1–15.8	
Wilson et al. (2014a) and	$\langle\beta_{e,tot}\rangle_{up}$	*THEMIS*	BS		∼0.39–17.2
Wilson et al. (2014b)	$\langle\beta_{e,tot}\rangle_{dn}$				∼0.64–5.97
Adrian et al. (2016)	$\beta_{e,\parallel}$	*Wind*	Slow SW	∼0.02 to >10	
	$\beta_{e,\parallel}$		Fast SW	∼0.05 to >10	
Bale et al. (2013)	$\beta_{e,tot}$		SW	∼0.01 to >100	
Chen et al. (2016)	$\beta_{e,\parallel}$			∼0.03 to >100	
Hull et al. (2001)	$\langle\beta_{e,tot}\rangle_{up}$		BS		∼1.5
	$\langle\beta_{e,tot}\rangle_{dn}$				∼1.4
Wilson et al. (2009)	$\beta_{ec,\parallel}$		IPS	∼0.70–1.16	
Wilson et al. (2010)	$\beta_{e,tot}$			∼0.55–11.5	
	$\beta_{ec,\parallel}$			∼0.1–8.0	
Wilson et al. (2012)	$\beta_{ec,\parallel}$			∼0.52–1.80	∼1.35

Table 17
(Continued)

Reference	Parameter	Spacecraft	Notes	X_{min}–X_{max}	$\bar{X}$
Wilson et al. (2013b)	$\beta_{ec,\parallel}$			∼0.20–1.05	
Wilson et al. (2013a)	$\beta_{ec,tot}$		IFS	∼0.1 to >100	
	$\beta_{eh,tot}$			∼0.1 to >400	
Wilson et al. (2018)	$\beta_{e,tot}$		SW	∼0.006–8870	∼2.31
	$\beta_{e,\parallel}$			∼0.005–8848	
	$\beta_{e,\perp}$			∼0.007–8914	
	$\beta_{e,tot}$		Slow SW	∼0.01–4329	∼3.35
	$\beta_{e,\parallel}$			∼0.01–4328	∼3.33
	$\beta_{e,\perp}$			∼0.01–4332	∼3.41
	$\beta_{e,tot}$		Fast SW	∼0.02–680	∼1.05
	$\beta_{e,\parallel}$			∼0.02–665	∼1.00
	$\beta_{e,\perp}$			∼0.02–710	∼1.16
This work	$\beta_{ec,\parallel}$	*Wind*	IPS/AT	∼0.05–3313	∼3.62
	$\beta_{ec,\perp}$			∼0.04–3268	∼3.51
	$\beta_{ec,tot}$			∼0.05–3283	∼3.54
	$\beta_{eh,\parallel}$			∼0.0001–375	∼0.48
	$\beta_{eh,\perp}$			∼0.0008–378	∼0.49
	$\beta_{eh,tot}$			∼0.0009–377	∼0.49
	$\beta_{eb,\parallel}$			∼0.00002–34	∼0.13
	$\beta_{eb,\perp}$			∼0.00003–46	∼0.12
	$\beta_{eb,tot}$			∼0.00003–42	∼0.12
	$\beta_{eff,\parallel}$			∼0.001–3721	∼4.15
	$\beta_{eff,\perp}$			∼0.001–3693	∼4.04
	$\beta_{eff,tot}$			∼0.001–3702	∼4.08

Notes. Definitions/symbols are the same as in Table 14. For symbol definitions, see Appendix A.
[a] HCU ≡ *Helios 1*, *Cluster*, and *Ulysses* spacecraft.

Table 18
Measurements of Electron Temperature Anisotropies at 1 au

Reference	Parameter	Spacecraft	Notes	X_{min}–X_{max}	$\bar{X}$
Lacombe et al. (2014)	$\mathcal{A}_e$	*Cluster*	SW	∼0.5–1.1	
Lacombe et al. (2017)	$\mathcal{A}_e$			∼0.57–1.0	
Viñas et al. (2010)	$\mathcal{A}_e$			∼1.0	
	$\mathcal{A}_{eb}$			∼0.5–4.0	
Lefebvre et al. (2007)	$\langle\mathcal{A}_e\rangle_{up}$		BS		∼0.61–0.93
	$\langle\mathcal{A}_e\rangle_{dn}$				∼0.91–1.07
Lazar et al. (2017)	$\mathcal{A}_{eh}$	HCU[a]	SW	∼0.25–1.75	
Štverák et al. (2008)	$\mathcal{A}_{ec}$	HC[b]	Slow SW	∼0.4–1.5	
	$\mathcal{A}_{eh}$			∼0.5–1.5	
	$\mathcal{A}_{ec}$		Fast SW	∼0.45–1.1	
	$\mathcal{A}_{eh}$			∼0.55–1.2	
Schwenn (1990)	$\mathcal{A}_e$	HCI[c]	SW		∼0.83
	$\mathcal{A}_e$		Slow SW		∼0.62
	$\mathcal{A}_e$		Fast SW		∼0.85
Feldman et al. (1973)	$\langle\mathcal{A}_e\rangle_{up}$	*Imp 6*	BS	∼0.67–1.00	
Feldman et al. (1975)	$\mathcal{A}_{ec}$	*Imp 7* and *8*	SW		∼1.06–1.10
	$\mathcal{A}_{eh}$				∼1.22–1.31
Feldman et al. (1978)	$\mathcal{A}_e$	*Imp 6*, *7*, and *Imp 8*	Fast SW		∼0.67
	$\mathcal{A}_{ec}$				∼0.80
	$\mathcal{A}_{eh}$				∼0.50
Feldman et al. (1979)	$\mathcal{A}_e$		SW	<0.69 to >0.95	
	$\mathcal{A}_{ec}$			∼0.79 to >0.97	
	$\mathcal{A}_{eh}$			<0.50 to >0.87	
Phillips et al. (1989b)	$\mathcal{A}_{ec}$	*ISEE 3*	SW	∼0.30 to >1.0	
	$\mathcal{A}_{eh}$			∼0.25 to >1.0	

Table 18
(Continued)

Reference	Parameter	Spacecraft	Notes	X_{min}–X_{max}	$\bar{X}$
Phillips et al. (1989a)	$\mathcal{A}_{ec}$			∼0.7–1.16	
Adrian et al. (2016)	$\mathcal{A}_e$	*Wind*	Slow SW	∼0.4–2.0	
	$\mathcal{A}_e$		Fast SW	∼0.3–3.0	
Crooker et al. (2003)	$\mathcal{A}_{eh}$		SW	∼0.1–100	
Salem et al. (2003)	$\mathcal{A}_e$			∼0.6–1.1	
Wilson et al. (2013a)	$\mathcal{A}_e$		IFS[d]	∼0.50–2.00	
	$\mathcal{A}_{ec}$			∼0.40–1.50	
	$\mathcal{A}_{eh}$			∼0.30–1.40	
Pulupa et al. (2010)	$\langle\mathcal{A}_e\rangle_{up}$		IPS	∼0.50–1.10	
Wilson et al. (2009)	$\mathcal{A}_{ec}$			∼0.70–1.11	
	$\mathcal{A}_{eh}$			∼0.55–1.14	
Wilson et al. (2010)	$\mathcal{A}_e$			∼0.55–1.30	
	$\mathcal{A}_{ec}$			∼0.55–1.35	
	$\mathcal{A}_{eh}$			∼0.55–1.80	
Wilson et al. (2012)	$\mathcal{A}_{ec}$			∼0.81–1.09	∼0.97
	$\mathcal{A}_{eh}$			∼0.81–1.29	∼0.995
Wilson et al. (2013b)	$\mathcal{A}_e$			∼0.75–1.31	
	$\mathcal{A}_{ec}$			∼0.73–1.30	
	$\mathcal{A}_{eh}$			∼0.75–1.76	
This work	$\mathcal{A}_{ec}$	*Wind*	IPS/AT	∼0.38–1.56	∼0.93
	$\mathcal{A}_{eh}$			∼0.24–15.0	∼1.06
	$\mathcal{A}_{eb}$			∼0.13–15.2	∼1.00
	$\mathcal{A}_{eff}$			∼0.35–2.80	∼0.93

Notes. Definitions/symbols are the same as in Table 14. For symbol definitions, see Appendix A.
[a] HCU ≡ *Helios 1*, *Cluster*, and *Ulysses* spacecraft.
[b] HC ≡ *Helios 1* and *Cluster*.
[c] HCI ≡ *Helios 1* and *2* and *Imp 7* and *8*.
[d] IFS ≡ terrestrial ion foreshock.

The electron velocity moments presented in Wilson et al. (2018), in contrast, were derived from multicomponent fits to the electron distribution observed by the *Wind* 3DP instrument (i.e., same data as used in this three-part study). Here the fits were performed on the one-dimensional cuts of the assumed two-dimensional gyrotropic distribution in logarithmic space (see Paper I for more details). Once the core, halo, and beam/strahl fit parameters were calculated, they were combined to form a total model distribution function similar to $f_s^{(mod)}$ discussed herein. The total model was numerically integrated to yield the electron velocity moments for the entire distribution function, analogous to that discussed in Appendix B herein. However, this data set explicitly excludes burst mode and so does not have a large number of solutions in the ±2 hr time window around IP shock ramps. Thus, the results presented in this three-part study are different in both scope and approach/technique.

ORCID iDs

Lynn B. Wilson, III https://orcid.org/0000-0002-4313-1970
Li-Jen Chen https://orcid.org/0000-0002-4768-189X
Shan Wang https://orcid.org/0000-0002-6783-7759
Steven J. Schwartz https://orcid.org/0000-0003-0682-2753
Drew L. Turner https://orcid.org/0000-0002-2425-7818
Michael L. Stevens https://orcid.org/0000-0002-7728-0085
Justin C. Kasper https://orcid.org/0000-0002-7077-930X
Adnane Osmane https://orcid.org/0000-0003-2555-5953
Damiano Caprioli https://orcid.org/0000-0003-0939-8775
Stuart D. Bale https://orcid.org/0000-0002-1989-3596
Marc P. Pulupa https://orcid.org/0000-0002-1573-7457
Chadi S. Salem https://orcid.org/0000-0002-6536-1531
Katherine A. Goodrich https://orcid.org/0000-0002-4288-5084

References

Adrian, M. L., Viñas, A. F., Moya, P. S., & Wendel, D. E. 2016, ApJ, 833, 49
Anderson, B. R., Skoug, R. M., Steinberg, J. T., & McComas, D. J. 2012, JGRA, 117, A04107
Anderson, K. A. 1981, JGRA, 86, 4445
Anderson, K. A., Lin, R. P., Martel, F., et al. 1979, GeoRL, 6, 401
Bale, S. D., Pulupa, M., Salem, C., Chen, C. H. K., & Quataert, E. 2013, ApJL, 769, L22
Ball, L., & Melrose, D. B. 2001, PASA, 18, 361
Bame, S. J., Asbridge, J. R., Gosling, J. T., et al. 1979, SSRv, 23, 75
Caprioli, D., & Spitkovsky, A. 2014, ApJ, 783, 91
Chen, C. H. K., Matteini, L., Schekochihin, A. A., et al. 2016, ApJL, 825, L26
Chen, L.-J., Wang, S., Wilson, L. B., III, et al. 2018, PhRvL, 120, 225101
Coroniti, F. V. 1970, JPlPh, 4, 265
Crooker, N. U., Larson, D. E., Kahler, S. W., Lamassa, S. M., & Spence, H. E. 2003, GeoRL, 30, 1619
Crooker, N. U., & Pagel, C. 2008, JGRA, 113, 2106
Feldman, W. C., Anderson, R. C., Bame, S. J., et al. 1983a, JGRA, 88, 96
Feldman, W. C., Anderson, R. C., Bame, S. J., et al. 1983b, JGRA, 88, 9949
Feldman, W. C., Asbridge, J. R., Bame, S. J., & Gosling, J. T. 1979, JGRA, 84, 7371
Feldman, W. C., Asbridge, J. R., Bame, S. J., Gosling, J. T., & Lemons, D. S. 1978, JGRA, 83, 5285
Feldman, W. C., Asbridge, J. R., Bame, S. J., & Montgomery, M. D. 1973, JGRA, 78, 3697

Feldman, W. C., Asbridge, J. R., Bame, S. J., Montgomery, M. D., & Gary, S. P. 1975, JGRA, 80, 4181
Fitzenreiter, R. J., Ogilvie, K. W., Bale, S. D., & Viñas, A. F. 2003, JGRA, 108, 1415
Gary, S. P., Scime, E. E., Phillips, J. L., & Feldman, W. C. 1994, JGRA, 99, 23391
Gary, S. P., Skoug, R. M., & Daughton, W. 1999, PhPl, 6, 2607
Gershman, D. J., Dorelli, J. C., F.-Viñas, A., & Pollock, C. J. 2015, JGRA, 120, 6633
Goodrich, K. A., Ergun, R. E., Schwartz, S. J., et al. 2018, JGRA, 123, 9430
Goodrich, K. A., Ergun, R. E., Schwartz, S. J., et al. 2019, JGRA, 124, 1855
Graham, G. A., Rae, I. J., Owen, C. J., & Walsh, A. P. 2018, ApJ, 855, 40
Graham, G. A., Rae, I. J., Owen, C. J., et al. 2017, JGRA, 122, 3858
Gurgiolo, C., & Goldstein, M. L. 2016, AnGeo, 34, 1175
Gurgiolo, C., Goldstein, M. L., Viñas, A. F., & Fazakerley, A. N. 2012, AnGeo, 30, 163
Harten, R., & Clark, K. 1995, SSRv, 71, 23
Hernandez, R., & Marsch, E. 1985, JGRA, 90, 11062
Hinton, F. L. 1984, in Basic Plasma Physics: Selected Chapters, ed. A. A. Galeev & R. N. Sudan (Amsterdam: North-Holland Publishing), 147
Hobara, Y., Balikhin, M., Krasnoselskikh, V., Gedalin, M., & Yamagishi, H. 2010, JGRA, 115, 11106
Horaites, K., Boldyrev, S., Wilson, L. B., III, Viñas, A. F., & Merka, J. 2018, MNRAS, 474, 115
Hull, A. J., & Scudder, J. D. 2000, JGRA, 105, 27323
Hull, A. J., Scudder, J. D., Fitzenreiter, R. J., et al. 2000, JGRA, 105, 20957
Hull, A. J., Scudder, J. D., Frank, L. A., Paterson, W. R., & Kivelson, M. G. 1998, JGRA, 103, 2041
Hull, A. J., Scudder, J. D., Larson, D. E., & Lin, R. 2001, JGRA, 106, 15711
Kajdič, P., Alexandrova, O., Maksimovic, M., Lacombe, C., & Fazakerley, A. N. 2016, ApJ, 833, 172
Kasper, J. C., & Klein, K. G. 2019, ApJL, 877, L35
Kasper, J. C., Klein, K. G., Weber, T., et al. 2017, ApJ, 849, 126
Kasper, J. C., Lazarus, A. J., Steinberg, J. T., Ogilvie, K. W., & Szabo, A. 2006, JGRA, 111, 3105
Kasper, J. C., Maruca, B. A., Stevens, M. L., & Zaslavsky, A. 2013, PhRvL, 110, 091102
Kasper, J. C., Stevens, M. L., Korreck, K. E., et al. 2012, ApJ, 745, 162
Kellogg, P. J. 1962, JGRA, 67, 3805
Kennel, C. F., Edmiston, J. P., & Hada, T. 1985, GMS, 34, 1
Krall, N. A., & Trivelpiece, A. W. 1973, Principles of Plasma Physics (San Francisco, CA: San Francisco Press)
Krauss-Varban, D., & Wu, C. S. 1989, JGRA, 94, 15367
Lacombe, C., Alexandrova, O., & Matteini, L. 2017, ApJ, 848, 45
Lacombe, C., Alexandrova, O., Matteini, L., et al. 2014, ApJ, 796, 5
Lazar, M., Shaaban, S. M., Poedts, S., & Štverák, Š. 2017, MNRAS, 464, 564
Lefebvre, B., Schwartz, S. J., Fazakerley, A. F., & Décréau, P. 2007, JGRA, 112, 9212
Lepping, R. P., Acũna, M. H., Burlaga, L. F., et al. 1995, SSRv, 71, 207
Leroy, M. M., & Mangeney, A. 1984, AnGeo, 2, 449
Lever, E. L., Quest, K. B., & Shapiro, V. D. 2001, JGR, 28, 1367
Lin, R. P. 1998, SSRv, 86, 61
Lin, R. P., Anderson, K. A., Ashford, S., et al. 1995, SSRv, 71, 125
Livadiotis, G. 2015, JGRA, 120, 1607
Livadiotis, G. 2017, J. Phys. Conf. Ser., 900, 012014
Maksimovic, M., Pierrard, V., & Riley, P. 1997, JGR, 24, 1151
Maksimovic, M., Zouganelis, I., Chaufray, J.-Y., et al. 2005, JGRA, 110, 9104
Marsch, E. 2006, LRSP, 3, 1
Marsch, E., & Livi, S. 1985, PhFl, 28, 1379
Maruca, B. A., & Kasper, J. C. 2013, AdSpR, 52, 723
Maruca, B. A., Kasper, J. C., & Bale, S. D. 2011, PhRvL, 107, 201101
Masters, A., Schwartz, S. J., Henley, E. M., et al. 2011, JGRA, 116, A10107
Mazelle, C., Lembège, B., Morgenthaler, A., et al. 2010, in Proc. AIP Conf. 1216, 12th Int. Solar Wind Conf., ed. M. Maksimovic et al. (Melville, NY: AIP), 471
Nicolaou, G., Livadiotis, G., Owen, C. J., Verscharen, D., & Wicks, R. T. 2018, ApJ, 864, 3
Nieves-Chinchilla, T., & Viñas, A. F. 2008, JGRA, 113, A02105
Ogilvie, K. W., Chornay, D. J., Fritzenreiter, R. J., et al. 1995, SSRv, 71, 55
Ogilvie, K. W., Fitzenreiter, R., & Desch, M. 2000, JGRA, 105, 27277
Pagel, C., Crooker, N. U., & Larson, D. E. 2005a, GeoRL, 32, 14105
Pagel, C., Crooker, N. U., Larson, D. E., Kahler, S. W., & Owens, M. J. 2005b, JGRA, 110, 1103
Pagel, C., Gary, S. P., de Koning, C. A., Skoug, R. M., & Steinberg, J. T. 2007, JGRA, 112, 4103
Park, J., Caprioli, D., & Spitkovsky, A. 2015, PhRvL, 114, 085003
Paschmann, G., & Daly, P. W. 1998, ISSIR, 1
Petschek, H. E. 1958, RvMP, 30, 966
Phillips, J. L., Gosling, J. T., McComas, D. J., Bame, S. J., & Smith, E. J. 1989a, JGRA, 94, 13377
Phillips, J. L., Gosling, J. T., McComas, D. J., et al. 1989b, JGRA, 94, 6563
Pilipp, W. G., Muehlhaeuser, K., Miggenrieder, H., Rosenbauer, H., & Schwenn, R. 1990, JGRA, 95, 6305
Pulupa, M. P., Bale, S. D., & Kasper, J. C. 2010, JGRA, 115, 4106
Pulupa, M. P., Bale, S. D., Salem, C., & Horaites, K. 2014, JGRA, 119, 647
Roberg-Clark, G. T., Drake, J. F., Reynolds, C. S., & Swisdak, M. 2016, ApJL, 830, L9
Roberg-Clark, G. T., Drake, J. F., Swisdak, M., & Reynolds, C. S. 2018, ApJ, 867, 154
Sagdeev, R. Z. 1966, RvPP, 4, 23
Salem, C., Bosqued, J.-M., Larson, D. E., et al. 2001, JGRA, 106, 21701
Salem, C., Hubert, D., Lacombe, C., et al. 2003, ApJ, 585, 1147
Schunk, R. W. 1975, P&SS, 23, 437
Schunk, R. W. 1977, RvGSP, 15, 429
Schwartz, S. J., Henley, E., Mitchell, J., & Krasnoselskikh, V. 2011, PhRvL, 107, 215002
Schwartz, S. J., & Marsch, E. 1983, JGRA, 88, 9919
Schwartz, S. J., Thomsen, M. F., Bame, S. J., & Stansberry, J. 1988, JGRA, 93, 12923
Schwenn, R. 1990, in Large-Scale Structure of the Interplanetary Medium, ed. R. Schwenn & E. Marsch (Berlin: Springer), 99
Scime, E. E., Phillips, J. L., & Bame, S. J. 1994, JGRA, 99, 14769
Scudder, J. D., & Karimabadi, H. 2013, ApJ, 770, 26
Scudder, J. D., & Olbert, S. 1979, JGRA, 84, 6603
Shizgal, B. D. 2018, PhRvE, 97, 052144
Skoug, R. M., Feldman, W. C., Gosling, J. T., McComas, D. J., & Smith, C. W. 2000, JGRA, 105, 23069
Song, P., Zhang, X. X., & Paschmann, G. 1997, P&SS, 45, 255
Spitzer, L., & Härm, R. 1953, PhRv, 89, 977
Štverák, S., Maksimovic, M., Trávníček, P. M., et al. 2009, JGRA, 114, 5104
Štverák, S., Trávníček, P., Maksimovic, M., et al. 2008, JGRA, 113, 3103
Tao, J., Wang, L., Zong, Q., et al. 2016a, in Proc. AIP Conf. 1720, SOLAR WIND 14, ed. L. Wang et al. (Melville, NY: AIP), 070006
Tao, J., Wang, L., Zong, Q., et al. 2016b, ApJ, 820, 22
Thomsen, M. F., Gosling, J. T., Bame, S. J., & Mellott, M. M. 1985, JGRA, 90, 137
Thomsen, M. F., Gosling, J. T., Onsager, T. G., & Russell, C. T. 1993, JGRA, 98, 3875
Thomsen, M. F., Stansberry, J. A., Bame, S. J., Gosling, J. T., & Mellott, M. M. 1987, JGRA, 92, 10119
Tidman, D. A., & Krall, N. A. 1971, Shock Waves in Collisionless Plasmas (New York: Wiley)
Tong, Y., Bale, S. D., Salem, C., & Pulupa, M. 2018, arXiv:1801.07694
Tong, Y., Vasko, I. Y., Artemyev, A. V., Bale, S. D., & Mozer, F. S. 2019a, ApJ, 878, 41
Tong, Y., Vasko, I. Y., Pulupa, M., et al. 2019b, ApJL, 870, L6
Treumann, R. A. 2009, A&ARv, 17, 409
Vandas, M. 2001, JGRA, 106, 1859
Vasko, I. Y., Krasnoselskikh, V., Tong, Y., et al. 2019, ApJL, 871, L29
Viñas, A. F., Gurgiolo, C., Nieves-Chinchilla, T., Gary, S. P., & Goldstein, M. L. 2010, in Proc. AIP Conf. 1216, 12th Int. Solar Wind Conf., ed. M. Maksimovic et al. (Melville, NY: AIP), 265
Walsh, A. P., Arridge, C. S., Masters, A., et al. 2013, JGR, 40, 2495
Wang, L., Lin, R. P., Salem, C., et al. 2012, ApJL, 753, L23
Wicks, R. T., Alexander, R. L., Stevens, M. L., et al. 2016, ApJ, 819, 6
Wilson, L. B., III, Cattell, C., Kellogg, P. J., et al. 2007, PhRvL, 99, 041101
Wilson, L. B., III, Cattell, C. A., Kellogg, P. J., et al. 2009, JGRA, 114, 10106
Wilson, L. B., III, Cattell, C. A., Kellogg, P. J., et al. 2010, JGRA, 115, 12104
Wilson, L. B., III, Chen, L.-J., Wang, S., et al. 2019a, ApJS, 243, 8
Wilson, L. B., III, Chen, L.-J., Wang, S., et al. 2019b, Supplement to: Electron Energy Partition across Interplanetary Shocks, v1.0, Zenodo, doi:10.5281/zenodo.2875806
Wilson, L. B., III, Koval, A., Sibeck, D. G., et al. 2013a, JGRA, 118, 957
Wilson, L. B., III, Koval, A., Szabo, A., et al. 2012, GeoRL, 39, 8109
Wilson, L. B., III, Koval, A., Szabo, A., et al. 2013b, JGRA, 118, 5
Wilson, L. B., III, Koval, A., Szabo, A., et al. 2017, JGRA, 122, 9115
Wilson, L. B., III, Sibeck, D. G., Breneman, A. W., et al. 2014a, JGRA, 119, 6455
Wilson, L. B., III, Sibeck, D. G., Breneman, A. W., et al. 2014b, JGRA, 119, 6475
Wilson, L. B., III, Stevens, M. L., Kasper, J. C., et al. 2018, ApJS, 236, 41
Wu, C. S. 1984, JGRA, 89, 8857